ACCEPTED MANUSCRIPT

Physics of Thermionic, Orificed Hollow Cathodes. Part 1: Theory and Experimental Validation

Physics of Thermionic, Orificed Hollow Cathodes. Part 1: Theory and Experimental Validation

P-Y C R Taunay, C J Wordingham and E Y Choueiri

Electric Propulsion and Plasma Dynamics Laboratory, Princeton University, Princeton, NJ 08544, USA

E-mail: ptaunay@princeton.edu,cjw4@alumni.princeton.edu

Abstract. A model aimed at illuminating the physics of thermionic, orificed hollow cathodes is developed and validated with experimental data. The model is intended to describe the variation of total (neutrals, ions, and electrons) static pressure with controllable parameters. That pressure must be properly evaluated because it influences important plasma parameters in the cathode such as the attachment length and the electron temperature, which directly impact the lifetime of thermionic inserts. The model, which combines a zero-dimensional approach to the conservation of energy and momentum for the combined plasma-neutral fluid and a charge-exchange-limited ambipolar diffusion model, allows for the computation of all plasma quantities, including the total fluid pressure. The model depends on the operating conditions (discharge current and mass flow rate), cathode geometry, and the gas species, along with two non-controllable parameters: the neutral gas temperature and the sheath potential. Total pressure data at up to 307 A of cathode discharge current were obtained experimentally and were used, along with data from the literature, to validate the model. Good agreement is obtained for all quantities. The model is used in a companion paper to clarify the role of magnetic and gasdynamic pressure in the scaling of total pressure, to derive scaling laws applicable to thermionic, orificed hollow cathodes, and to propose novel cathode design rules.

Physics of Thermionic, Orificed Hollow Cathodes. Part 1: Theory and Experimental Validation

2

1. Introduction

Thermionic, orificed hollow cathodes serve as plasma sources of electrons and have been used for a variety of applications, such as surface processing [1–3], neutral beam injectors for fusion devices [4–6], and electric space propulsion [7, 8]. They feature a hollow tube (made of either a refractory metal or graphite) which is capped by an orifice plate and in which a low-work-function thermionic material is inserted. A keeper electrode is placed around and/or in front of the cathode to initiate the discharge and to protect the orifice plate from high-energy ions (hypothesized to be generated by ion acoustic instabilities in the plume [9]) that are accelerated towards the cathode. An external heater is used to bring the insert material to emitting temperatures. The cathode is surrounded by heat shields to reduce radiative losses. A neutral gas (*e.g.*, xenon) is then introduced into the tube and a discharge is established with the keeper or an external anode.

Because orificed hollow cathodes are the most promising type of cathodes for future space missions, their reliable operation is critical. Proposed space propulsion applications require operational lifetimes of up to 100,000 hours (100 kh) [10,11] without servicing, with estimated total discharge powers in the range of 100–200 kW [12]. This is equivalent to up to 800 A of discharge current for a typical Hall-effect thruster (assuming an efficiency of 100%, a specific impulse of 2,000 s, and xenon gas). Existing thrusters are starting to approach or exceed this power level [13–15]. To date, however, only cathodes that operate at low current (< 20 A) have undergone life testing and the lifetime of high-current (> 100 A) cathodes has only been estimated to be in the tens of kilo-hours (see Figure 1). There is a clear need for technological improvements to increase cathode performance to a combined range of discharge current and lifetime that can enable next-generation missions. High discharge currents can be achieved by scaling the cathodes to larger sizes. It is unclear, however, how the cathode lifetime is affected by an increase in discharge power.

The lifetime of thermionic orificed hollow cathodes is limited by the erosion of its external surfaces and, fundamentally, by the evaporation and sputtering of the thermionic emitter. Both processes depend on the behavior of the plasma in the insert region. Sputtering of the emitter material is not a primary
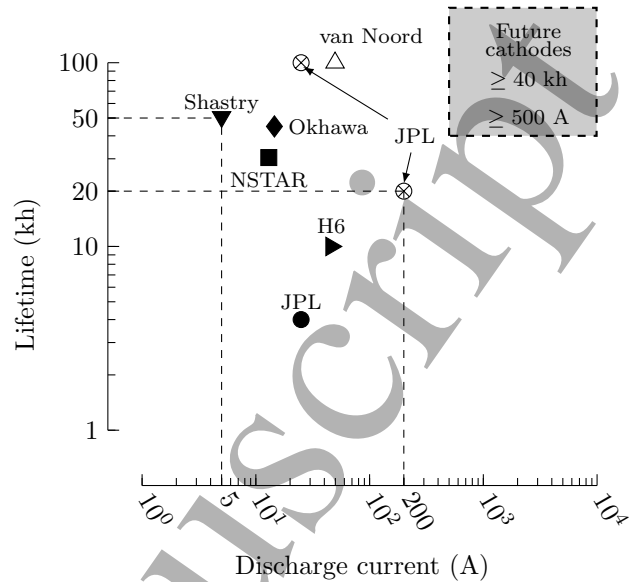
Figure 1: Demonstrated (solid) and estimated (open) lifetime of hollow cathodes for given discharge currents. Original data from [16–22]. None of the cathodes for which lifetime testing was conducted reached end-of-life. Reproduced from "Pierre-Yves C. R. Taunay, *Scaling Laws in Orificed Thermionic Hollow Cathodes,* Ph.D. dissertation, Princeton University, 2020." [23] Copyright 2020, Pierre-Yves C. R. Taunay.

concern for typical cathode operation, as the sputtering yield of typical thermionic emitters is low enough to prevent sputtering of the emitter material (this is true for sheath potentials of less than 20 V) [24, 25]. To limit evaporation low-temperature (~1000°C) operation of the emitter is preferable. This can be achieved by increasing the attachment length (*i.e.*, the plasma contact with the emitter) to reduce the insert temperature for a given discharge current [26, 27]. The attachment length, or length over which the plasma is dense enough to "absorb" all emitted electrons, is a direct measure of the plasma coupling to the emitter. The attachment length and electron temperature are affected by experimentally controllable parameters (*e.g.*, mass flow rate, discharge current) in a complex fashion. We seek to explain this behavior through simple models that cover most cathode operating regimes (*i.e.*, low to high discharge current and mass flow rate).

Physics of Thermionic, Orificed Hollow Cathodes. Part 1: Theory and Experimental Validation   3

The neutral gas pressure in an orificed hollow cathode affects physical quantities such as the ratio of sheath-edge plasma density to average plasma density and electron temperature [28, 29], and, therefore, the total lifetime of the insert. In the insert region, under the assumptions of charge-exchange-dominated ambipolar diffusion and spatially constant electron temperature and pressure, it can be shown that the electron temperature depends only on the geometry of the cathode and the neutral gas density (or pressure for a constant temperature) [29, 30]. These assumptions are typically valid for orificed hollow cathodes. It is critical to obtain an accurate value of the neutral gas pressure to ensure that the lifetime of the thermionic insert is maximized.

To estimate the neutral gas pressure, both the total pressure and ionization fraction can be used. Multiple approaches exist to estimate the total pressure, many of which are used within the context of a zero-dimensional cathode model: empirical relationships, designed for a mercury hollow cathode [31–36] or based on the available data from the literature [37], isentropic [38] or isothermal [39, 40] flow approaches, Poiseuille flow theory [30, 41, 42], a modification of Poiseuille flow theory [43, 44], and an "equivalent temperature" or modified specific gas constant taking into account the ionization fraction [39,40,45,46]. We have shown in [37] that the empirical relationships developed in [31–36] do not generalize to other cathodes and that the assumptions of isentropic, isothermal, or viscous Poiseuille flow are invalid in the flow regime in which cathodes operate. The empirical relationship we proposed in [37] covers available data from the literature but may not generalize to new designs unless they are similar to cathodes included in the analysis used to derive the relationship. It is also limited by its data-driven approach which does not explain the physical phenomena governing the total pressure in orificed hollow cathodes.

A two-dimensional computational approach may be used to evaluate the plasma quantities within hollow cathodes. This type of approach include two-dimensional fluid [47–52], coupled plasma-thermal [53], hybrid-particle in cell (PIC) [54, 55], and full PIC models [56,57]. Such framework can provide the spatial variation of all simulated quantities and may be used for detailed cathode design and derivation of scaling laws. However, scaling laws may also be derived from simpler approaches. Through well-justified simplifying assumptions, we provide an alternative approach to the calculation of plasma quantities to describe the variation of the total pressure with controllable parameters and, ultimately, develop scaling laws applicable to hollow cathodes. To the authors' knowledge, no idealized approach such as the one we

present here has been *(i)* applied to a wide range of cathode operating conditions, or *(ii)* used to study the scaling of the total pressure (as shown in our companion paper).

We have shown in [28] that existing 0-D models [30–35, 38, 41–46, 58–65] cannot be applied to cathodes that are different from the design for which they were originally developed. It is therefore not possible to use those models for a wide variety of cathodes and operating conditions.

We propose in this work to use the combination of zero-dimensional, volume-averaged, conservation equations for all species (ions, electrons, neutrals) present in the cathode and a two-dimensional charge-exchange-limited ambipolar diffusion model for the electrons, which is solved analytically. The latter model was presented in [29]. We then discuss the required assumptions we make and delineate the theoretical model. We finally demonstrate that the results of the model agree with experimental data of total pressure, electron temperature, attachment length, and wall temperature on a variety of cathodes that span a range of 1–307 A of discharge current, 3.7–109 sccm of mass flow rate, and multiple gases and geometries.

2. Experiment

2.1. Cathode configuration

The Princeton large hollow cathode (PLHC) is a 20 cm (8 in.) long cathode with an inner bore of 3.26 cm (1.284 in.). The cathode material is AXM-5Q POCO graphite. The PLHC features two 2.715 cm inner diameter, 4.02 cm long lanthanum hexaboride (LaB$_6$) inserts for a total of 8.04 cm length. The inserts are heated via an external graphite heater described in [66]. The heater is insulated from the cathode with a set of boron nitride (BN) insulator rings. A heat shield made of multiple layers of 200 μm (0.008 in.) thick grafoil and of 50 μm (0.002 in.) thick molybdenum is used to reduce radiative heat loss. The cathode has a tungsten orifice plate which is 1.5 mm thick and which has a 5.6 mm (7/32 in.) diameter orifice. The cathode is mounted on a block of 253MA stainless steel and is held in place by a clamp ring of the same material. The clamp ring is fastened to the cathode base with 1/4"-20 screws. Interfaces between materials are sealed with grafoil gaskets. Downstream of the cathode orifice are a 6.35 mm (1/4 in.) thick graphite keeper plate with a 9.52 mm (3/8 in.) diameter orifice and a water-cooled, aluminum anode. The keeper plate is held in front of the cathode with a combination of stainless steel and ceramic posts. The keeper is attached to the stainless steel posts with #6-32 screws. The ceramic posts are fastened to the cathode base with #6-32 screws and to

Physics of Thermionic, Orificed Hollow Cathodes. Part 1: Theory and Experimental Validation

4

the stainless steel post with #6-32 threaded rods.

Gas flows through the cathode through a stainless steel compression tube fitting (Swagelok-to-NPT fitting) mounted on the side of the cathode base. A pressure tap is drilled into the cathode base opposite the gas inlet and provides a direct connection to a Baratron gauge situated outside the vacuum facility. Both gas inlet and pressure tap fittings are sealed with an anti-seizing compound. The seal on the back of the cathode is provided by a grafoil gasket between the cathode base and a structure ("diagnostics pod") that houses additional plasma diagnostics not used in this study. Design details of the diagnostics pod can be found in [67]. Figure 2 shows an exploded view of the cathode assembly (without fasteners) as rendered by a computer-aided design (CAD) software, along with a table showing the materials used for each component. Both a CAD drawing and cutaway view of
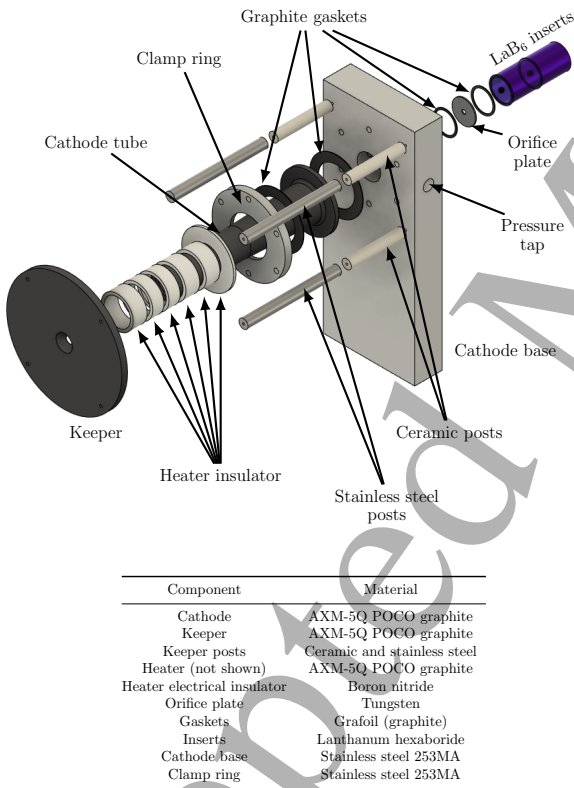

(a) Front view.

(b) Right view.

(c) Top view.

(d) Isometric view. The gas inlet (hidden in this view) is situated opposite of the pressure tap.

Figure 3: CAD rendering of the cathode without heater, fasteners, and heat shields. Dimensions are in cm. Reproduced from "Pierre-Yves C. R. Taunay, *Scaling Laws in Orificed Thermionic Hollow Cathodes,* Ph.D. dissertation, Princeton University, 2020." [23] Copyright 2020, Pierre-Yves C. R. Taunay.

cathode, anode, and heater. The cathode, with keeper and heat shielding installed, is shown in Figure 6b.

2.2. Facilities

The cathode is installed in a 2 m diameter by 5 m long fiberglass vacuum vessel evacuated to less than 7×10^{-5} Torr (0.01 Pa, 1 mbar) without gas flow, or 2×10^{-4} Torr (0.03 Pa, 3.2 mbar) at the maximum tested flow rate (8.6 mg/s or 290 sccm of argon), by a pair of 1.2 m (48 in.) diameter diffusion pumps backed by a roots blower and two roughing pumps. The graphite heater is powered by a 13.3 kW power supply with a maximum output of 32 V or 400 A. In all of our experiments the cathode operates in triode mode (cathode, keeper, anode). The cathode discharge is sustained by a 30 kW welding power supply configured for a maximum output of 150 V or 500 A. The total current from the power supply is controlled with a manual dial. An electrical diagram of the setup is shown in Figure 7.

The anode and keeper current are provided by the same power supply. Our heater is able to provide

Figure 2: Exploded view of the cathode assembly without heater, fasteners, and heat shields. Reproduced from "Pierre-Yves C. R. Taunay, *Scaling Laws in Orificed Thermionic Hollow Cathodes,* Ph.D. dissertation, Princeton University, 2020." [23] Copyright 2020, Pierre-Yves C. R. Taunay.

Component	Material
Cathode	AXM-5Q POCO graphite
Keeper	AXM-5Q POCO graphite
Keeper posts	Ceramic and stainless steel
Heater (not shown)	AXM-5Q POCO graphite
Heater electrical insulator	Boron nitride
Orifice plate	Tungsten
Gaskets	Grafoil (graphite)
Inserts	Lanthanum hexaboride
Cathode base	Stainless steel 253MA
Clamp ring	Stainless steel 253MA

the cathode without heater, heat shields, and fasteners can be found in Figure 3 and Figure 4, respectively. We show in Figure 5 a schematic of the experimental setup and in Figure 6a a photograph of the actual
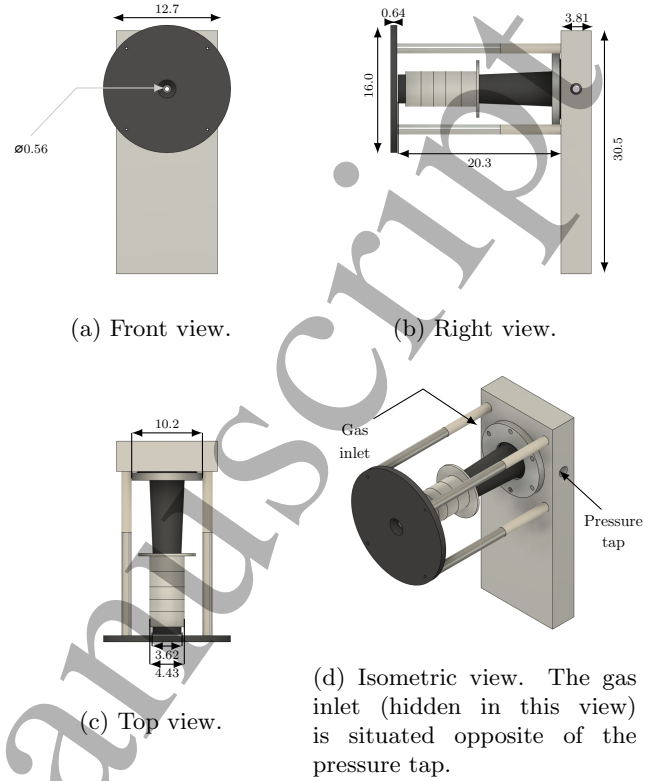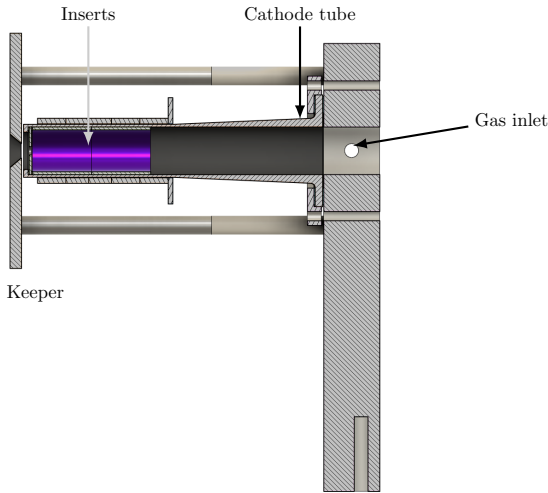
Figure 4: Cutaway view of the cathode assembly showing the location of the installed inserts and gas inlet. Reproduced from "Pierre-Yves C. R. Taunay, *Scaling Laws in Orificed Thermionic Hollow Cathodes,* Ph.D. dissertation, Princeton University, 2020." [23] Copyright 2020, Pierre-Yves C. R. Taunay.

Figure 5: Schematic of the cathode apparatus (top view) showing the location of temperature measurements. Adapted from "Pierre-Yves C. R. Taunay, *Scaling Laws in Orificed Thermionic Hollow Cathodes,* Ph.D. dissertation, Princeton University, 2020." [23] Copyright 2020, Pierre-Yves C. R. Taunay.
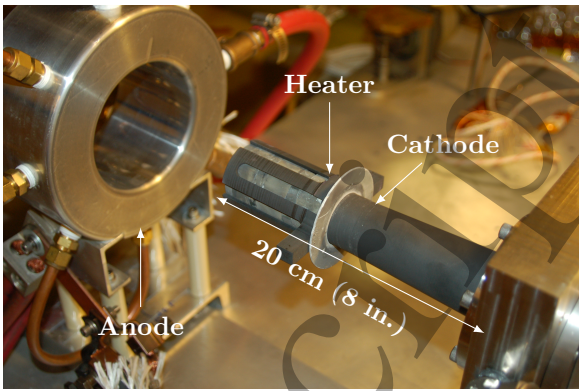
(a)
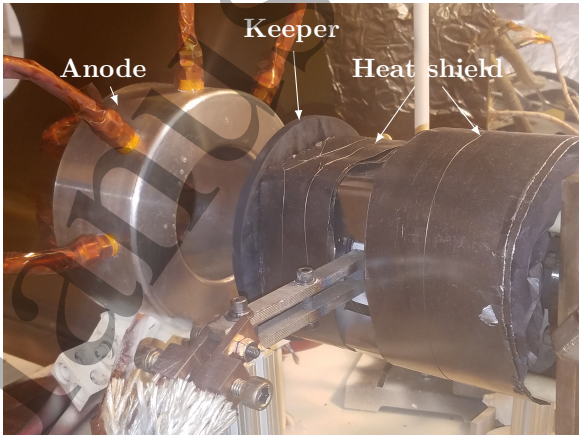
(b)

Figure 6: Princeton large hollow cathode (a) without and (b) with heat shields. Adapted from "Pierre-Yves C. R. Taunay, *Scaling Laws in Orificed Thermionic Hollow Cathodes,* Ph.D. dissertation, Princeton University, 2020." [23] Copyright 2020, Pierre-Yves C. R. Taunay.

current flowing through the cathode, anode, keeper, and heater, respectively.

2.3. Measurement system

Pressure We measure the total pressure upstream of the cathode with an MKS 622C baratron gauge connected to the stainless steel support block through a 3/8 in. NPT fitting. The pressure tap is located approximately 22 cm (8.75 in.) from the upstream surface of the cathode orifice. The gauge is situated outside the vacuum tank, another 1.2 m away from the pressure tap. A National Instruments (NI) data acquisition system is used to perform a differential voltage measurement across the Baratron gauge output.

enough power to ensure that the ignition voltage falls below the maximum voltage of the 30 kW power supply. A 50 Ω resistor is used in series with the keeper to limit the total keeper current to 3 A.

The experimental circuit features resistor shunts R_c, R_a, R_k, and R_h that are used to measure the
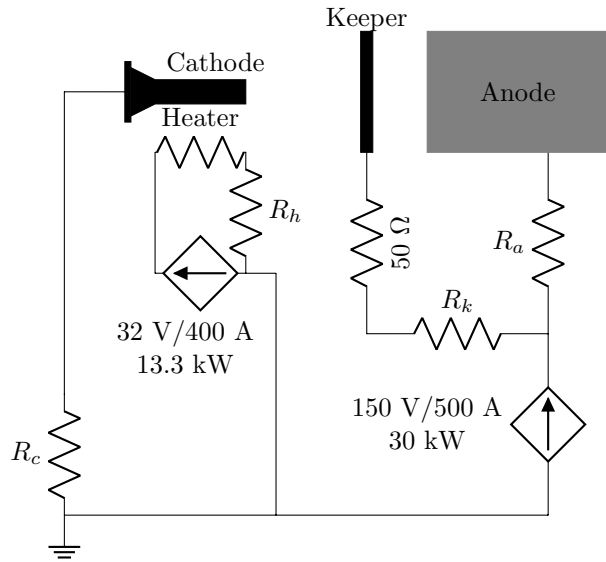
Figure 7: Electrical diagram of the experiment. Reproduced from "Pierre-Yves C. R. Taunay, *Scaling Laws in Orificed Thermionic Hollow Cathodes,* Ph.D. dissertation, Princeton University, 2020." [23] Copyright 2020, Pierre-Yves C. R. Taunay.

Temperature During operation, we measure the temperature of the cathode tip and of one of the tabs of the heater with C-type thermocouples that are in direct contact with either surface. A K-type thermocouple is used to evaluate the temperature of the stainless steel base. The location of the temperature measurements is shown in Figure 5.

2.4. Total pressure measurements

Figure 8 shows pressure measurements we performed with and without the cathode discharge. Without a plasma, the pressure increases linearly with mass flow rate as is expected from a choked orifice. During operation the pressure increases both with mass flow rate and discharge current, a behavior similar to other cathodes [36, 68, 69].

3. Theory

3.1. Assumptions

We make the following assumptions:

(i) In the insert and orifice regions, the ionized species are treated as a continuum fluid.

(ii) The heavy-particle stagnation temperature in both regions is constant and is a free parameter.

(iii) The flow in the orifice is frozen.

(iv) The total static pressure is constant in the insert region.
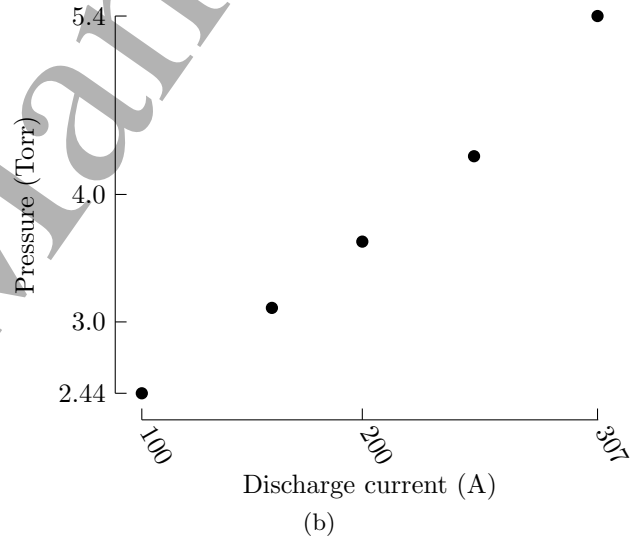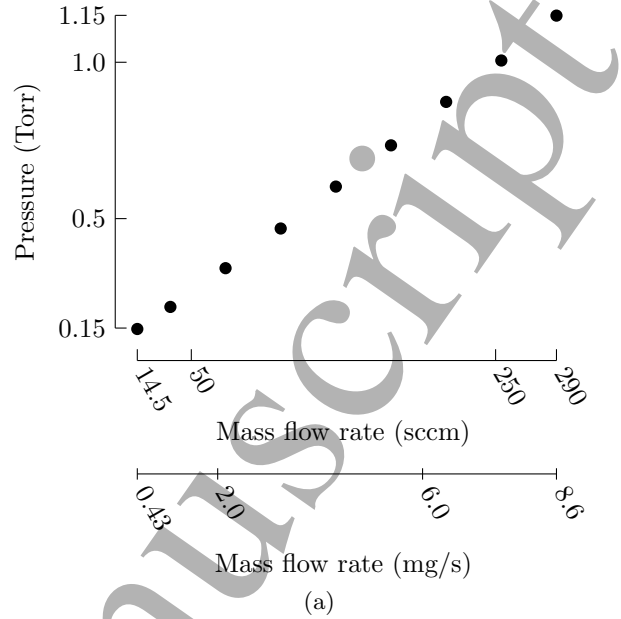
Figure 8: Total pressure measurements: (a) with cold gas only (300 K, no discharge: $I_d = 0$ A); (b) during cathode operation, at 109 sccm of argon, and discharge current of 100–307 A. Adapted from "Pierre-Yves C. R. Taunay, *Scaling Laws in Orificed Thermionic Hollow Cathodes,* Ph.D. dissertation, Princeton University, 2020." [23] Copyright 2020, Pierre-Yves C. R. Taunay.
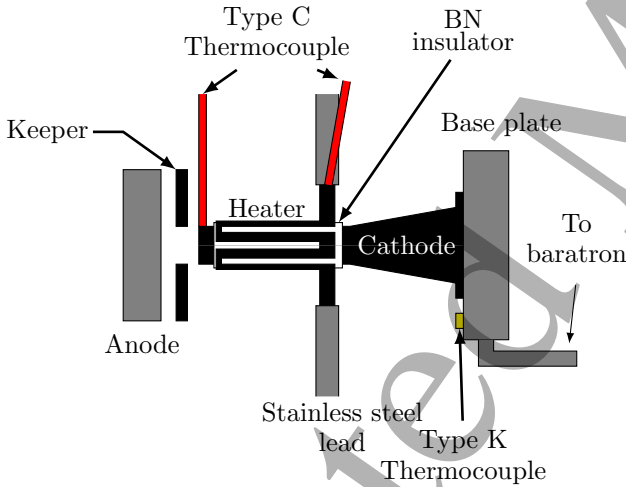
(v) The flux of ions to the walls is equal to the Bohm flux and is not modified by the presence of an emitting sheath.

(vi) The fluid is inviscid.

(vii) The electron temperature is constant in each region.

(viii) The electron inertia is negligible compared to that of the heavy species.

Physics of Thermionic, Orificed Hollow Cathodes. Part 1: Theory and Experimental Validation   7

(ix) Inelastic collisions other than direct ionization and ground-state excitation are ignored.

(x) Steady-state conditions are reached.

Our first assumption is justified in the insert region of cathodes with a small orifice-to-insert diameter ratio (*i.e.*, most orificed hollow cathodes) [37]. The Knudsen number is generally less than 1 for those cathodes. This assumption is invalid when the flow becomes transitional, such as in the cathode orifice, in cathodes that have an orifice-to-insert diameter ratio close to 1 (*i.e.*, tube cathodes), and in cathodes with a sufficiently low mass flow rate (depending on the orifice size [30], p.270). We will use empirical corrections to compensate for transitional flow effects at the orifice outlet. The second assumption implies that the ion and neutral static temperatures are equal, which is justified for heavy species that have a large cross section for resonant charge exchange (*e.g.*, noble gases). We specify the static temperature in the orifice region and calculate the stagnation temperature under the assumption of an adiabatic flow. This assumption is used in 0-D cathode models [30, 38, 41, 42, 58–61, 63, 64, 70, 71] and the model we describe here is not sensitive to the value of the neutral gas temperature in the range of 2,000–4,000 K. Some 2-D computational models [48–50] also assume that the ion and neutral temperatures are identical. The results of other two-dimensional computational models [49,52] show that the temperature of the heavy species is not identical for every spatial location: the heavy species may not only have a different temperature, but also have a spatial temperature variation. For example, numerical results from [52] indicate that the on-axis neutral temperature varies from 3,000 K to 2,550 K upstream of the orifice over a range equal to the insert radius (0.2 cm). However, the *volume-averaged* neutral and ion temperatures are near-identical: in the active region upstream of the orifice, the results from [52] indicate that they are equal to 2,490 K and 2,480 K, respectively (assuming an emission length, to first order, equal to the insert radius: $L_{\text{eff}} \approx r_c$). In general, it is challenging to experimentally obtain the temperature of the neutral particles or ions in either the insert or orifice regions, and it is therefore difficult to unambiguously evaluate the validity of the second assumption. This assumption nonetheless simplifies the theoretical approach.

Because the mean free path for inelastic electron-neutral collisions is much larger than the orifice size, and because the residency time is smaller than the time between inelastic collisions for neutral particles in the orifice, the assumption of frozen flow (assumption iii) is justified, for typical operating conditions. The ratios of mean free path to orifice length L_o and inter-collision

time to residency time for the neutrals are given by:

$$\bar{\lambda} = \frac{1}{n_e \sigma\left(T_{eV}\right) L_o},\tag{1}$$

and

$$\bar{\tau} = \frac{v_g}{L_o}\left(n_e \left\langle \sigma\left(T_{eV}\right) v\right\rangle\right)^{-1} = \frac{v_g}{v_e}\bar{\lambda},\tag{2}$$

respectively. In Equations (1) and (2), n_e is the electron density, σ is the inelastic collision cross section, T_{eV} is the electron temperature in eV, v_g is the local sound speed, and v_e is the electron thermal velocity. Figure 9 shows the two ratios for xenon and two orifice aspect ratios Λ_{or} (orifice length over orifice diameter), where we assume a gas temperature of 2,000 K to calculate the speed of sound. The electron temperature is calculated from the neutral gas density using the ambipolar diffusion model from [29]. The total excitation cross section is the sum of the ground-state excitation collision cross sections. The mean free path for inelastic collisions is much longer than the orifice length for all neutral densities of interest. As indicated by the variation of the ratio of inter-collision time to neutral gas residency time, the frozen flow approximation may be challenged for large orifice aspect ratios. The likelihood that a neutral atom undergoes many inelastic collisions before exiting the orifice channel is then very high. In general, however, this approximation allows us to provide a bound on the flow variables.

Assuming a constant total static pressure (assumption iv) in the insert region is justified because pressure gradients are small in the insert region for cathodes with small orifice-to-insert-diameter ratio. Pressure gradients, however, can exist far from the orifice inlet, where the flow is constricted, as has been demonstrated by 2-D simulations [49, 57]. The flow gains dynamic pressure at the expense of static pressure in this region. The pressure difference between the upstream section and the orifice plate results in an additional force which increases the momentum flux through the orifice [72]. Ignoring this effect should result in an under-prediction of the total pressure. This result is also a consequence of our usage of *volume-averaged* quantities. Because our control volume is drawn near the orifice inlet, and because pressure gradients exist near the orifice inlet, a volume average will likely yield a value which is below that of the upstream one.

It is necessary to estimate the flux of ions to the walls to include particle effects in the fluid model. Assuming that ions achieve the Bohm velocity at the edge of an emitting sheath (assumption v) is not necessarily justified [28] but it is a common assumption to most cathode models (including 2-D computational models [51]). Using the model from [73] it is possible

Physics of Thermionic, Orificed Hollow Cathodes. Part 1: Theory and Experimental Validation   8

Figure 9: Ratio of (a) mean free path to orifice length for total inelastic electron-neutral collisions, (b) inter-collision t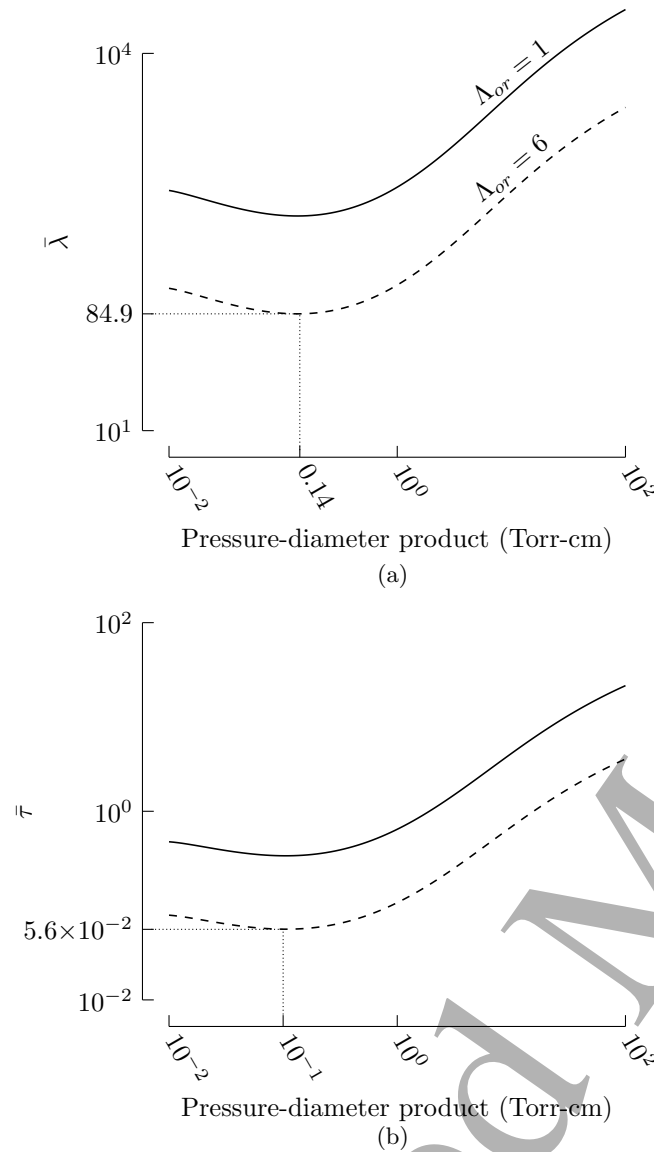ime to neutral gas residency time. Reproduced from "Pierre-Yves C. R. Taunay, *Scaling Laws in Orificed Thermionic Hollow Cathodes,* Ph.D. dissertation, Princeton University, 2020." [23] Copyright 2020, Pierre-Yves C. R. Taunay.

to estimate the modification of the Bohm velocity by an emitting sheath:

$$v_{\text{ion}} = \left(\frac{eT_{eV}}{M}\right)^{1/2}\left(\frac{1 + 2\eta_c J_b}{1 - J_b}\right)^{1/2}, \tag{3}$$

where $\eta_c = \phi_s/T_{eV}$ is the normalized sheath voltage, $J_b = j_b/j_e$, where j_b is the emitted beam current and j_e is the electron saturation current:

$$j_e = n_e e\left(\frac{eT_{eV}}{m}\right)(2\eta_c)^{3/2}. \tag{4}$$

For cathodes that have a small orifice-to-insert-diameter ratio, the ion current through the sheath is negligible as compared to the emitted electron (beam) and electron saturation currents because of low sheath voltages ($\eta_c \propto 1$) and high plasma densities (10^{20}–10^{21} m^{-3}) [30]. In this case, the ratio of the beam current to the electron saturation current is typically negligible ($J_b \ll 1$), and, therefore, so is the modification to the Bohm velocity. However, under certain circumstances, the presence of an emitting sheath may modify the Bohm velocity by up to 20%. We consider in this case that the sheath boundary is situated farther away from the wall at a location where the Bohm velocity is reached. Because the size of the sheath ($\propto \mu$m) is much smaller than the scale of the system ($\propto$ cm) this increase of the effective sheath size does not affect the diffusion characteristics of the solution.

Through a dimensional and statistical analysis of experimental data, the study in [37] showed that the gasdynamic and plasma effects can account for most of the variation in the total pressure within hollow cathodes. We therefore neglect the effect of viscosity on the total pressure gradient. We caution that viscosity may nonetheless affect other quantities, such as the neutral flow velocity profile (see, *e.g.*, Fig. 7 in [49]), and that our approach cannot capture effects beyond volume-averaged ones. Viscosity can nonetheless be implemented by considering that most of the viscous losses come from the feed system.

Experimental measurements of the pressure data we used are gathered upstream of the insert region (sometimes multiple cathode lengths away, see, *e.g.*, [43]). This means that the viscous pressure drop within the feed system contributes to the measured total pressure. In most cases, feed-system losses are negligible. Feed-system losses are estimated to be less than 0.01% of the measured pressure for Domonkos's cathodes (see [43], p. 26). Using a Poiseuille flow model upstream of the active zone and assuming an upper bound for the temperature of 1,000 K, the feed-system loss can be estimated to be, on average, 3%, for the NSTAR, NEXIS, JPL 1.5 cm, PLHC, and Salhi's cathodes. For those cathodes, the pressure measurement point is situated less than 20 cm away from the cathode active zone. A Poiseuille flow assumption is justified in the section upstream of the plasma (as suggested by [49] for the NSTAR cathode and a single operating condition) and within the feed system: the flow is neutral, isothermal, viscous, laminar, incompressible, fully-developed, and not near a constriction. We use the heavy-particle temperature

Physics of Thermionic, Orificed Hollow Cathodes. Part 1: Theory and Experimental Validation 9

as the effective gas temperature when estimating the viscous losses in the feed system.

Experimental data [22, 32, 40, 74, 75] for mercury, argon, and xenon gas suggest that the gradients of the electron temperature in the active zone of the insert and orifice regions are negligible, which indicates that assumption vii is appropriate. In effect, this assumption means that the fluid is isothermal in each individual region. Because the emitter electron return current is proportional to the Boltzmann factor ($j_e \propto \exp\left(-\phi_s/T_e\right)$), assumption vii introduces possible errors in the numerical evaluation of the return current. However, those errors do not seem to impact the evaluation of the emitter temperature. It is also difficult to evaluate the exact nature of the errors introduced in our model because, to the authors' knowledge, no experimental measurements of either the sheath voltage or the return electron current in the active zone of cathodes exist.

3.2. Fluid model

We use the two-dimensional axisymmetric momentum equations for each species, applied to the geometry shown in Figure 10. Boundaries II, III, and IV are chosen to be at the sheath edge. The effective attachment length (or "emission length"), L_{eff}, is the length over which the plasma is able to support temperature-limited thermionic emission. We approximate this length with the plasma density decay length scale in the axial direction, as calculated in [29]. As defined, it is a likely lower bound to the attachment length. The emission length, L_{eff}, is smaller than the insert length, L_{em}, and we consider that the fluid is neutral upstream of the emission zone.

The momentum equations for each species are summed to provide a simpler single-fluid framework. Under the assumptions delineated in the previous section, we obtain:

$$\nabla \cdot (\rho \boldsymbol{v v}) + \nabla P = \nabla \cdot \underline{\underline{\boldsymbol{\beta}}}, \tag{5}$$

where $\boldsymbol{v}$ is the mean mass velocity of the combined fluid, ρ its density, and $\underline{\underline{\boldsymbol{\beta}}}$ the magnetic stress tensor. P is the total static pressure. Equation (5) may also be written as

$$\nabla \cdot (M n_n \boldsymbol{v_n v_n} + M n_e \boldsymbol{v_i v_i}) + \nabla P = \nabla \cdot \underline{\underline{\boldsymbol{\beta}}}, \tag{6}$$

where the subscripts n, e, and i denote neutral, electron, and ion quantities, respectively. n_x and $\mathbf{v_x}$ are the number density and velocity of the species x, respectively. M is the mass of the heavy particles.

To satisfy conservation of mass, ions return to the control volume as neutrals after having recombined on any of the sheath-facing surfaces (II, III, and IV). The

flux of each species is therefore equal in magnitude and opposite in direction:

$$n_n v_n = -n_e^s v_B, \tag{7}$$

where n_e^s is the electron density at the sheath edge.

An upper-bound on the magnetic pressure on surfaces III and V can be obtained by considering that the magnetic field $\boldsymbol{B}$ on these surfaces is due only to the current flowing through the orifice, which is assumed to be purely axial. The magnetic field is then purely azimuthal:

$$\boldsymbol{B} = (0, B_\theta, 0)_{(\hat{r}, \hat{\theta}, \hat{z})}. \tag{8}$$

The magnetic stress tensor can then be expressed as [76]:

$$\underline{\underline{\boldsymbol{\beta}}} = \begin{bmatrix} -B_\theta^2/2\mu_0 & 0 & 0 \\ 0 & B_\theta^2/2\mu_0 r^2 & 0 \\ 0 & 0 & -B_\theta^2/2\mu_0 \end{bmatrix}, \tag{9}$$

where μ_0 is the permeability of vacuum. The azimuthal component of the magnetic field can be estimated by further assuming constant current density in the orifice:

$$B_\theta = \begin{cases} -\dfrac{\mu_0 I_d}{2\pi r} & \text{if } r > r_o \\[2mm] -\dfrac{\mu_0 I_d}{2\pi r_o^2} r & \text{if } r < r_o \end{cases} \tag{10}$$

where r_o is the orifice radius and I_d is the discharge current.

We integrate Equation (6) over the volume shown in Figure 10, and apply Gauss's theorem. In the z-direction, we obtain:

$$- \left[\pi r_c^2 P\right]_{\text{I}} + \pi \left(r_c^2 - r_o^2\right) \left[P + M n_e^s v_B^2 \left(\frac{n_e^s}{n_n} + 1\right)\right]_{\text{III}}$$

$$+ \pi r_o^2 \left[\rho v_z^2 + P\right]_{\text{V}} = -\frac{\mu_0 I_d^2}{4\pi} \left(\ln \frac{r_c}{r_o} + \frac{1}{4}\right), \tag{11}$$

where r_c is the insert radius and v_z is the fluid velocity on the surface V. To obtain Equation (11) we further assumed that

- the upstream (Surface I) momentum flux ($\left[\rho v_z^2\right]_{\text{I}}$) is negligible as compared to the static pressure contribution ($\left[P\right]_{\text{I}}$),

- for surfaces I, III, and V, surface quantities other than the magnetic field (*i.e.*, the pressure and momentum terms) are constant over their respective surfaces,

- the heavy particles have equal tangential velocity on each surface, and

- the radial velocity of the heavy particles on surface V is much smaller than the axial one.
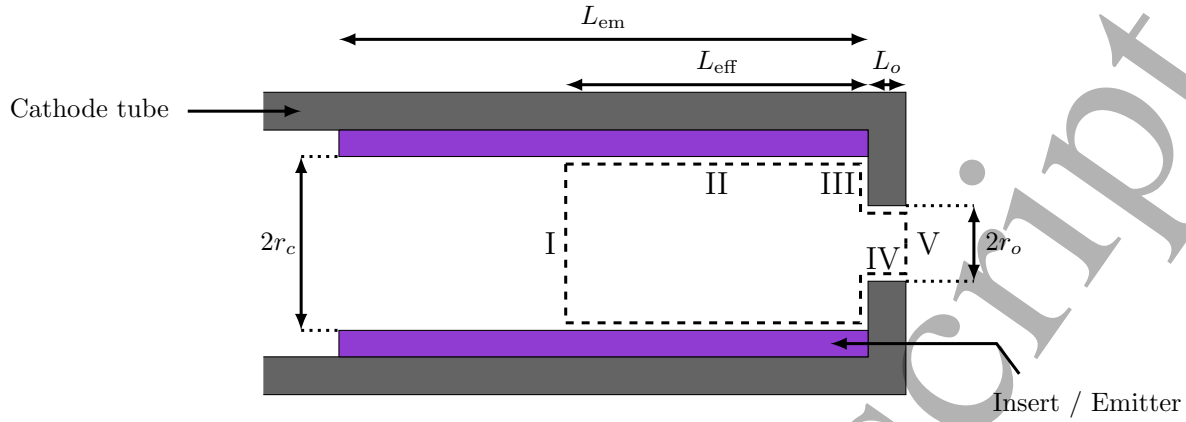
Physics of Thermionic, Orificed Hollow Cathodes. Part 1: Theory and Experimental Validation 10

Figure 10: Fluid control volume considered in the analysis. Adapted from "Pierre-Yves C. R. Taunay, *Scaling Laws in Orificed Thermionic Hollow Cathodes,* Ph.D. dissertation, Princeton University, 2020." [23] Copyright 2020, Pierre-Yves C. R. Taunay.

The first assumption is justified by using the continuity equation: $\rho v_z^2 = \left(\dot{m}/\pi r_c^2\right)^2 1/\rho$. The density, ρ can be approximated using the experimental pressure and an assumed gas temperature: $\rho \approx MP_I/\left(k_B T_n\right)$ Using the experimental cathode database presented in [77], we can compare ρv_z^2 to the measured (static) total pressure. The term ρv_z^2 represents *at most* 0.3% of the static pressure. This assumption cannot be performed at the outlet (Surface V) of the control volume because the flow is assumed to be sonic on this surface. Using a simple isentropic flow approach, the ratio of static to total pressure at the sonic point is given by:

$$\frac{P}{P_{\text{total}}} = \left(\frac{\gamma+1}{2}\right)^{-\gamma/(\gamma-1)}, \tag{12}$$

where γ is the ratio of heat capacities. For a monatomic gas ($\gamma = 5/3$) we obtain $\frac{P}{P_{\text{total}}} \approx 0.5$. The total force on the downstream surface (Surface V), therefore, is comprised of both the static contribution ($\pi r_o^2 [P]_{\text{V}}$) and the momentum flux term ($\pi r_o^2 [\rho v_z^2]_{\text{V}}$) as neither can be neglected.

The second assumption is *not* required on surfaces II and IV, as all terms in the momentum balance in the z direction vanish on those surfaces. Because the surfaces are oriented perpendicular to the axial direction, the pressure and the magnetic field components simply vanish in the vector dot-product. As demonstrated below, the dyad product also vanishes, even before the surface integration is performed.

The third assumption, combined with the flux condition given in Equation (7), causes the cross-term in the dyad product to vanish. For example, on surface II, the cross-term resulting from the momentum balance in the axial direction is:

$$S = Mn_e^s v_{i,r} v_{i,z} + Mn_n v_{n,r} v_{n,z}.$$

Because the particle fluxes normal to the wall are equal in magnitude and in opposite direction (Equation (7)), we have:

$$S = Mn_e^s v_B \left(v_{i,z} - v_{n,z}\right).$$

The assumption of equal tangential velocity, motivated by frequent collisions between ions and neutrals, implies that $v_{i,z} = v_{n,z}$ on this surface. The dyad terms then simplify to zero. $\square$

Outlet (surface V) The frozen-flow approximation allows us to define the Mach number and specific heat ratio γ. Under this assumption, the flow is choked and becomes sonic at the exit of the orifice because it expands into a vacuum. The flow velocity is therefore given by the local speed of sound a for the combined fluid:

$$v_{z,\text{V}} = a = \sqrt{\gamma R_g \left(T_n + \alpha T_e\right)}, \tag{13}$$

where R_g is the specific gas constant of neutral species, α is the ionization fraction, and T_n and T_e are the neutral and electron temperatures in Kelvin, respectively. This expression can be readily derived for an ideal gas where $a = \sqrt{\gamma P/\rho}$. The ionization fraction is defined as:

$$\alpha = \frac{n_e}{n_e + n_n}. \tag{14}$$

Using the conservation of mass, we also have $\pi r_o^2 \left(\rho v_z\right)_{\text{V}} = \dot{m}$.

Because the Knudsen number in the orifice, Kn, is within the range of 0.1 – 10 the flow is considered transitional. We therefore estimate P_{V} with a molecular flow correction. We use a similar framework to [78–80]. Under the justifiable assumption that the pressure downstream of the cathode orifice

Physics of Thermionic, Orificed Hollow Cathodes. Part 1: Theory and Experimental Validation 11

(vacuum vessel pressure) is much smaller than the exit plane pressure, the stagnation pressure P_V^* is given by

$$P_V^* = \frac{\dot{Q}}{(\theta C_m + (1-\theta) C_v)}, \tag{15}$$

where $\dot{Q}$ is the total throughput and C_{ta} is the total aperture conductance. The latter is given by:

$$C_{ta} = (\theta C_m + (1-\theta) C_v), \tag{16}$$

where C_m and C_v are the molecular flow and viscous flow aperture conductances, respectively. The linear weight θ is a function of the Knudsen number. The expression proposed in [78] can be written as suggested by [79] and [80]:

$$\theta = \frac{k_\theta \mathrm{Kn}}{k_\theta \mathrm{Kn} + 1}, \tag{17}$$

where $k_\theta = 28$. This value of k_θ corresponds to equal weighing of molecular and viscous flows ($\theta \approx 0.5$) when the average pressure in the orifice is equal to the midpoint pressure of the transition range [78]. This corresponds to $\mathrm{Kn} \approx 0.04$. The throughput and the conductance of the orifice aperture for the flow are given by:

$$\dot{Q} = \frac{k_B}{M} T_n \left(\frac{\gamma+1}{2} \right) \dot{m}, \text{ and} \tag{18a}$$

$$C_a = \pi r_o^2 \sqrt{\left(\frac{\gamma+1}{2} \right) \frac{k_B T_n}{2\pi M}}, \tag{18b}$$

respectively. The $(\gamma+1)/2$ term comes from the conversion from static to stagnation quantities in the insert region. Because the throughput is referenced to upstream stagnation quantities, the plasma contribution to the sound speed does not appear in $\dot{Q}$. The molecular and viscous flow conductances are [78, 79]

$$C_m = C_a \left(\frac{2}{\gamma+1} \right)^{1/2}, \text{ and} \tag{19a}$$

$$C_v = \sqrt{2\pi} \left(\gamma \left(\frac{2}{\gamma+1} \right)^{(\gamma+1)/(\gamma-1)} \right)^{1/2} C_a, \tag{19b}$$

respectively. The static pressure on surface V is retrieved from the definition of the stagnation pressure at a Mach number of 1:

$$P_V = P_V^* \left(\frac{2}{\gamma+1} \right)^{\gamma/(\gamma-1)}. \tag{20}$$

We show in Figure 11 the total conductance of a thin aperture as obtained with Santeler's approach [78] (Equation (16)) normalized by the molecular flow conductance of an aperture (Equation (19a)) as a function of Knudsen number, and compare it to experimental and numerical results for argon, helium, and krypton from [81] and [82], respectively. Because the experimental and numerical results only consider

two quiescent volumes separated by a thin aperture, the upstream stagnation and static quantities are identical and we do not consider the term $(\gamma+1)/2$ (conversion from static to stagnation quantities in the insert region) in the above equations for this comparison. The discrepancy observed at low Knudsen
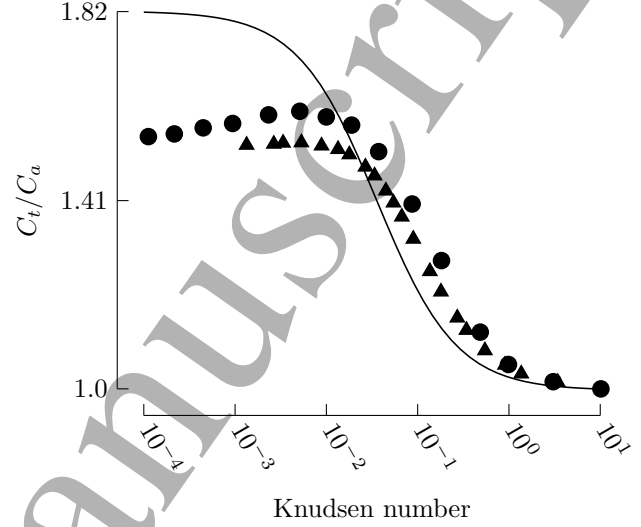
Figure 11: Comparison of transition flow model to experimental and numerical results from [81] and [82], respectively.

numbers stems from the fact that we did not include the discharge coefficient (estimated to be ≈ 0.835 [81, 82]) in the calculation of the conductance in the viscous regime. In the range of Knudsen number of interest (0.1–10), the empirical relationship features a relative error of less than 12% and 10% as compared to both experimental and numerical results, respectively.

Orifice plate (surface III) Because we have assumed a constant total pressure in the insert volume, the total static pressure on the orifice plate is equal to that at the inlet: $P_{III} = P_I$.

Total pressure We reorganize Equation (11) to obtain an expression for the total (static) pressure:

$$P = P_{mag} + P_{gd} + P_{mf} + P_{\text{exit}} \tag{21}$$

where P_{mag}, P_{gd}, P_{mf}, P_{exit} are the magnetic pressure on surfaces III and V, gasdynamic pressure contribution, orifice plate momentum flux, and orifice outlet exit pressure, respectively. These quantities are defined as:

$$P_{mag} = \frac{\mu_0 I_d^2}{4\pi^2 r_o^2} \left(\ln \frac{r_c}{r_o} + \frac{1}{4} \right), \tag{22a}$$

$$P_{gd} = \frac{\dot{m}}{\pi r_o^2} \sqrt{\gamma R_g (T_n + \alpha_o T_e)}, \tag{22b}$$

Physics of Thermionic, Orificed Hollow Cathodes. Part 1: Theory and Experimental Validation 12

$$P_{mf} = \left(\frac{r_c^2}{r_o^2} - 1\right) e n_e^s T_{eV} \left(1 + \frac{n_e^s}{n_n}\right), \text{ and} \qquad (22c)$$

$$P_{\text{exit}} = P_V^* \left(\frac{2}{\gamma + 1}\right)^{\gamma/(\gamma-1)}, \qquad (22d)$$

respectively. P_{mf}, n_e^s and T_{eV} are calculated using insert-region quantities. The speed of sound of the fluid appearing in the gasdynamic pressure is computed with orifice-region quantities. α_o denotes the ionization fraction in the orifice. Equation (21) states that the total static pressure upstream of the cathode emission zone is the balance between the particle momentum leaving the volume, the magnetic pressure, and the downstream static pressure.

The total pressure in the absence of plasma effects ($P_{mf} = P_{mag} = 0$) for a continuum flow ($\theta = 0$) is:

$$P = \frac{\dot{m}}{\pi r_o^2} \sqrt{\gamma R_g T_n} \left(1 + \frac{1}{\gamma}\right). \qquad (23)$$

This expression is different from the one that would be obtained with an isentropic flow relationship:

$$P_{\text{isentropic}} = \frac{\dot{m}}{\pi r_o^2} \sqrt{\gamma R_g T_n} \frac{1}{\gamma} \left(\frac{\gamma + 1}{2}\right)^{\gamma/(\gamma-1)}. \qquad (24)$$

For a monatomic gas, the constants $(1 + 1/\gamma)$ and $1/\gamma \left((\gamma + 1)/2\right)^{\gamma/(\gamma-1)}$ that appear in Equations (23) and (24) are equal to 1.6 and 1.23, respectively. The discrepancy comes from the assumption that the static pressure on the orifice plate (surface III) is equal to the upstream total pressure. This assumption of a pressure force on the orifice plate is fundamentally inconsistent with the derivation of isentropic flow relationships, as the use of the momentum balance combined with this assumption over-determines the system of flow equations. In practice, isentropic flow relationships are derived from the energy and continuum equations, with the momentum balance being used to find the total pressure force on the control volume (or the thrust, for nozzle flows). In the absence of a plasma, simple isentropic flow relationships should be directly used to estimate the total pressure inside the cathode.

3.3. Plasma model

To close the system of equations, estimates of the degree of ionization, neutral density, and electron temperature are required for both the insert and orifice regions. In the insert region an estimate of the attachment length, or length over which the plasma is dense enough to support temperature-limited thermionic emission, is also required. Because the ionization fraction may not be negligible (especially in the orifice region) we do not employ the typical approximation $\alpha \ll 1$; we retain all terms in the resulting equations in both regions. For all of our calculations, the collision frequencies are computed using Maxwellian-averaged collision cross sections.

3.3.1. Electron temperature and attachment length

We employ the method delineated in [29] to calculate the electron temperature in both insert and orifice regions, as well as the attachment length. The method is based on a charge-exchange-limited ambipolar diffusion model of the plasma. Application of this method gives an analytical approximation of the attachment length and the electron temperature in both regions as functions of the neutral-pressure-diameter product only. We define the "attachment length," more specifically, as the plasma density decay length-scale for the first-order eigenmode of the full 2-D solution in the insert. The insert electron temperature is not sensitive to the neutral gas temperature in that region; we therefore ran the 2-D solution with an assumed neutral gas temperature of 3,000 K in the insert region. The orifice electron temperature, however, can vary by up to 20% with a change in neutral gas temperature. The solution is therefore calculated with multiple neutral gas temperatures.

We use the following approximations for the insert and orifice electron temperature,

$$T_{eV}^{\text{insert}} = \frac{t_{i,0}}{(n_n k_B T_n (2r_c))^{t_{i,1}}} + t_{i,2}, \qquad (25a)$$

$$T_{eV}^{\text{orifice}} = \frac{t_{o,0}}{(n_n k_B T_n (2r_c))^{t_{o,1}} + t_{o,2}} + t_{o,3}, \qquad (25b)$$

and for the attachment length,

$$L_{\text{eff}} = r_c \left(l_0 + \frac{l_1}{(n_n k_B T_n (2r_c))^{l_2}}\right), \qquad (26)$$

respectively. The coefficients $t_{i,k}$, $t_{o,k}$, and l_k for xenon and argon gases are shown in the Appendix (Table A1). In all cases, the pressure-diameter product that appears in the denominator is in Torr-cm. The above expressions for the insert electron temperature and attachment length are compared to experimental data for a variety of cathodes in the companion paper.

The dependence of the electron temperature and electron density profile on the neutral pressure (*i.e.*, the neutral density for a fixed neutral temperature) and geometry can be seen in the eigenvalue equation that is obtained from the ambipolar diffusion framework. In 1-D, the electron density, n_e, is obtained with:

$$\frac{d^2 n_e}{dr^2} + \frac{1}{r}\frac{dn_e}{dr} + \frac{\nu_{iz}}{D_a} n_e = 0, \qquad (27)$$

where n_e is the plasma density, ν_{iz} is the ionization rate, and D_a is the ambipolar diffusion coefficient. Assuming a Dirichlet boundary condition at the wall (*i.e.*, zero plasma density) in a cylindrical geometry, the following eigenvalue equation is obtained from Equation 27 (see, *e.g.*, [30] pp. 63–65, [83] p. 165, [84] pp. 135–144):

$$\left(\frac{r_c}{\lambda_{01}}\right)^2 n_n \sigma_{iz}(T_{eV}) \sqrt{\frac{8eT_{eV}}{\pi m}} - D_a = 0, \qquad (28)$$

Physics of Thermionic, Orificed Hollow Cathodes. Part 1: Theory and Experimental Validation　　　　13

where λ_{01} is the first zero of the Bessel function of 0th order. Because of the inverse relationship between the ambipolar diffusion coefficient and the neutral gas density n_n for charge-exchange-dominated plasmas found in cathodes, it can be shown that, using Equation 28, the electron temperature depends only on the neutral density-radius product (*i.e.*, the pressure-diameter product for a fixed temperature). In the more general 2-D case treated in [29], a Robin boundary condition is used across a range of pressure-diameter products. The Robin boundary condition yields a transcendental equation that is similar to Equation (28) and that is tabulated for a range of pressure-diameter products for a given gas.

3.3.2. Insert region The conservation of charge in the insert region gives the total discharge current I_d as:

$$I_d = I_i + I_{em} - I_r, \tag{29}$$

where I_i, I_{em}, and I_r are the ion, thermionic, and random electron currents, respectively. Assuming that all ions created in the volume go to the insert wall, the ion current is either given by its volumetric definition, or by its value at the sheath edge,

$$I_i = e n_n n_e < \sigma_{iz} v > \pi L_{\text{eff}} r_c^2$$
$$= e n_e^s v_B 2 \pi r_c L_{\text{eff}}, \tag{30}$$

where σ_{iz} is the ionization cross-section. Using Equation (30), we obtain the sheath-edge density:

$$n_e^s = \frac{n_n n_e < \sigma_{iz} v > r_c}{2 v_B} = \frac{\alpha}{1-\alpha} \frac{n_n^2 < \sigma_{iz} v > r_c}{2 v_B}. \tag{31}$$

We use this result to define f_s, the ratio between the sheath-edge and the volume-averaged electron density, as a function of volume-averaged quantities:

$$f_s = \frac{n_e^s}{n_e} = \frac{n_n < \sigma_{iz} v > r_c}{2 v_B}. \tag{32}$$

The random electron current can also be expressed in terms of volumetric quantities by using the definition of the sheath-edge density (Equation (31)):

$$I_r = e \frac{1}{4} \left(\frac{8M}{\pi m} \right)^{1/2} n_n n_e < \sigma_{iz} v > \pi L_{\text{eff}} r_c^2$$
$$\times \exp \left(-\phi_s / T_{eV} \right), \tag{33}$$

where m is the mass of the electron and ϕ_s is the sheath potential.

We integrate the electron energy equation over a cylindrical volume of length L_{eff} and radius r_c with the face fluxes estimated using a zeroth-order upwind scheme as suggested in [30] (p.259). We obtain:

$$I_{em} \phi_s + R_p I_d^2 = q_{ex} + I_i \epsilon_i + \frac{5}{2} T_{eV} I_d$$
$$+ (2 T_{eV} + \phi_s) I_r, \tag{34}$$

where q_{ex} is the total power loss due to radiative transitions from ground-level, ϵ_i is the ionization

energy of the species of interest, and R_p is the plasma resistance. The power loss due to radiative transitions from ground level is given by the total excitation rate in the volume multiplied by the average energy of each transition:

$$q_{ex} = e n_e n_n < \sigma_{ex} v > \pi L_{\text{eff}} r_c^2 \epsilon_{ex}. \tag{35}$$

The excitation cross section in Equation (35) is the *total* cross section for all ground-state excitation reactions. The excitation energy is computed as the average of all excitation energies weighted by their respective Maxwellian-averaged reaction rates. The plasma resistance is given by:

$$R_p = \frac{m}{n_e e^2} \frac{L_{\text{eff}}}{\pi r_c^2} \left(\nu_{ei} + \nu_{en} \right), \tag{36}$$

where ν_{ei} and ν_{en} are the electron-ion and electron-neutral collision frequencies, respectively.

We use the conservation of charge (Equation (29)) to eliminate the thermionic current terms from the electron energy equation. This removes the dependency of the model on the chosen insert material and assumed wall temperature, although it introduces the unknown sheath potential, which we use as a free parameter. The resulting equation is expressed in terms of the ionization fraction and the neutral gas density by replacing the electron density with the definition of the ionization fraction (Equation (14)). This yields a quadratic expression for the unknown ionization fraction:

$$i_2 \alpha^2 + i_1 \alpha + i_0 = 0. \tag{37}$$

The coefficients i_k are functions of the cathode geometry, neutral gas density, sheath potential, and neutral gas temperature. They are given by:

$$i_2 = e n_n^2 < \sigma_{iz} v > \pi L_{\text{eff}} r_c^2$$
$$\times \left(\epsilon_i + \phi_s + 2 T_{eV} \frac{1}{4} \left(\frac{8M}{\pi m} \right)^{1/2} \exp \left(-\phi_s / T_{eV} \right) \right)$$
$$+ e n_n^2 < \sigma_{ex} v > \pi L_{\text{eff}} r_c^2 \epsilon_{ex}$$
$$+ \frac{m L_{\text{eff}}}{\pi r_c^2 e^2} C \ln \Lambda T_{eV}^{-3/2} I_d^2 - I_d \left(\frac{5}{2} T_{eV} - \phi_s \right)$$
$$- \frac{m L_{\text{eff}}}{\pi r_c^2 e^2} I_d^2 < \sigma_{en} v >, \tag{38a}$$

$$i_1 = I_d \left(\frac{5}{2} T_{eV} - \phi_s \right) - \frac{m L_{\text{eff}}}{\pi r_c^2 e^2} C \ln \Lambda T_{eV}^{-3/2} I_d^2$$
$$+ 2 \frac{m L_{\text{eff}}}{\pi r_c^2 e^2} I_d^2 < \sigma_{en} v >, \text{ and} \tag{38b}$$

$$i_0 = - \frac{m L_{\text{eff}}}{\pi r_c^2 e^2} I_d^2 < \sigma_{en} v >, \tag{38c}$$

where $C = 2.9 \times 10^{-12}$, and $\ln \Lambda \approx 10$ is the Coulomb logarithm. σ_{en} and σ_{ex} are the electron-neutral cross sections for elastic and excitation collisions, respectively. ϵ_{ex} is the average electron excitation

energy. We use data from the Hayashi database [85] as retrieved from the LXCat website [86] for the electron-neutral, ionization, and excitation cross sections.

3.3.3. Orifice region In the orifice, the energy equation can be considerably simplified by neglecting thermionic emission and electron backstreaming because of the higher sheath voltages due to the lower neutral densities than in the insert region. We again obtain a quadratic equation from the orifice energy balance:

$$o_2 \alpha^2 + o_1 \alpha + o_0 = 0, \tag{39}$$

where the coefficients o_k are:

$$o_2 = en_n^2 < \sigma_{iz} v > \pi L_o r_o^2 \epsilon_i + en_n^2 < \sigma_{ex} v > \pi L_o r_o^2 \epsilon_{ex}$$
$$+ \frac{mL_o}{\pi r_o^2 e^2} C \ln \Lambda T_{eV}^{-3/2} I_d^2 - \frac{mL_o}{\pi r_o^2 e^2} I_d^2 < \sigma_{en} v >$$
$$- \frac{5}{2} I_d \left(T_{eV} - T_{eV}^{\text{ins}} \right), \tag{40a}$$

$$o_1 = \frac{5}{2} I_d \left(T_{eV} - T_{eV}^{\text{ins}} \right) - \frac{mL_o}{\pi r_o^2 e^2} C \ln \Lambda T_{eV}^{-3/2} I_d^2$$
$$+ 2 \frac{mL_o}{\pi r_o^2 e^2} I_d^2 < \sigma_{en} v >, \text{ and} \tag{40b}$$

$$o_0 = - \frac{mL_o}{\pi r_o^2 e^2} I_d^2 < \sigma_{en} v > . \tag{40c}$$

L_o is the orifice length and T_{eV}^{ins} is the insert electron temperature.

To obtain a relationship between the ionization fraction and neutral density, we use the conservation of mass applied to the sonic condition at the orifice outlet. This results in a quadratic equation for the ionization fraction,

$$\dot{m} = \pi r_o^2 \frac{1}{1 - \alpha} n_n M \sqrt{\gamma R_g \left(T_n + \alpha T_e \right)}. \tag{41}$$

Solving this equation and selecting the root for which $\alpha_o < 1$ gives an expression for the ionization fraction,

$$\alpha = 1 + \frac{1}{2\bar{v}} \left(1 - \sqrt{4\bar{v} \left(1 + \bar{T} \right) + 1} \right), \tag{42}$$

where $\bar{T} = T_n / T_e$ and $\bar{v}$ is given by

$$\bar{v} = \frac{1}{\gamma R_g T_e} \left(\frac{\dot{m}}{\pi r_o^2 n_n M} \right)^2. \tag{43}$$

The orifice energy equation (Equation (39)) and the solution for the ionization fraction from conservation of mass (Equation (42)) are combined to obtain a single equation for the unknown neutral density in the orifice.

4. Implementation

4.1. Algorithm

Both the gas temperature and sheath voltage are free parameters. Three major advantages exist in using the

sheath voltage as a free parameter as opposed to the wall temperature: *(i)* the solution does not depend on the choice of emitter material, *(ii)* the sheath potential can be bounded, and *(iii)* the resulting solution algorithm is more stable because the thermionic current, which has a strong non-linear dependence on the wall temperature, has been eliminated from the volume-edge current balance (Equation (29)). In general, the sheath potential depends nonlinearly on the local plasma parameters and operating conditions through an elliptic PDE. The sheath potential problem is, therefore, non-local, and a self-consistent sheath model would therefore require a 2-D approach: this is beyond the scope of this work. The expression for the sheath-edge density ratio (Equation (32)) is used in the pressure balance (Equation (21)) to form an expression that depends only on α and n_n:

$$P = P_{mag} + P_{gd}$$
$$+ \left(\frac{r_c^2}{r_o^2} - 1 \right) f_s \frac{\alpha_i}{1 - \alpha_i} n_n e T_{eV} \left(1 + \left(\frac{\alpha_i}{1 - \alpha_i} \right) f_s \right)$$
$$+ P_{\text{exit}}. \tag{44}$$

To solve this equation, we use the perfect gas law to compute the total static pressure:

$$P = k_B n_n T_n + \frac{\alpha_i}{1 - \alpha_i} n_n e T_{eV} + \frac{\alpha_i}{1 - \alpha_i} n_n k_B T_n. \tag{45}$$

Because we have used surface-integrated quantities when deriving the pressure balance, but re-expressed these terms using volume-averaged quantities, there are (at least) two possible choices for the definition of the total static pressure. Assuming constant total pressure in the insert region, we can either use the sheath-edge density or the volumetric value of the density to compute this pressure. We choose the latter option because the sheath-edge terms balance the corresponding ones on the upstream portion, leaving only the pressure contribution on the orifice inlet.

Solving the system of equations resulting from the combination of the pressure balance (Equation (44)), the perfect gas law (Equation (45)), and the insert power balance (Equation (37)) yields the solution for both n_n and α_i. We combine the expressions into a single equation for the unknown neutral density which we then solve using the bisection method to avoid solving the original multivariate nonlinear system. For each proposed insert neutral density and sheath potential, we solve for the ionization fraction in the insert using the insert power balance (Equation (37)). The insert electron temperature is then obtained using the correlation in Equation (25a). The orifice neutral density is calculated using the orifice power balance (Equation (39)), mass continuity (Equation (42)), and the insert electron temperature. The electron temperature for the orifice is then obtained using Equation (25b), and the ionization fraction for the

Physics of Thermionic, Orificed Hollow Cathodes. Part 1: Theory and Experimental Validation   15

orifice is computed with Equation (42). Finally, the total pressure results calculated using the momentum balance (Equation (44)) and the perfect gas law (Equation (45)) are compared. If both results agree, the algorithm has converged and the solution is reported.

For a given geometry and gas, the orifice quantities depend on the mass flow rate, the discharge current, and the insert neutral density through the insert electron temperature. The orifice quantities can therefore be pre-computed and stored as a lookup table for faster computation. The upper bound for the orifice neutral density can be obtained by imposing the conditions that $\alpha_o > 0$ and that the neutral density in the insert is greater than that in the orifice. We check that both conditions are satisfied for each orifice neutral density found.

4.1.1. Wall temperature While the emission current has been eliminated from the model equations, the wall temperature may be retrieved from the total emitted current and the conservation of charge (Equation (29)). The elimination of the emitted current from the model equations also removes the dependence of the pressure on the choice of emitter material, excluding any indirect dependence due to the temperature of the heavy species.

The emitted current is first estimated from the input discharge current and the computed ion and electron return currents, I_i and I_r, respectively. Without the Schottky effect, the total emitted current is given by Richardson-Dushman's law,

$$I_{em} = 2\pi L_{\text{eff}} r_c D_{RD} T_c^2 \exp\left(-\frac{e\phi_w}{k_B T_c}\right), \qquad (46)$$

where D_{RD} is the Richardson-Dushman constant, T_c is the emitter temperature, and ϕ_w is the work function. Because we have assumed that the emission length is defined such that the thermionic emission is thermally limited inside the active zone, the current extracted is not modified by space-charge limitation. Because the control volume we chose is limited to the plasma "active zone," the computed wall temperature corresponds to the average insert temperature over a length equal to that of the emission length.

The attachment length provided by the ambipolar diffusion framework from [29] is a lower bound to the true attachment length. Because the emission area and, therefore, emission current, scales with the attachment length ($I_{em} \propto L_{\text{eff}}$), the obtained wall temperature will be an upper bound of the average active zone insert temperature. Uncertainties in the work function of some materials (*e.g.*, LaB$_6$ [53]) may also result in an over-estimation of the wall temperature. The evaporation rate of a given material will therefore also be over-estimated, and any lifetime

calculations that can be conducted with our framework will provide a conservative estimate of the evaporation-limited lifetime of the emitter.

4.1.2. Sheath potential The sheath potential depends nonlinearly on the local plasma parameters and operating conditions (*e.g.*, discharge current, anode voltage) through an elliptic PDE. As opposed to 2-D computational models, our approach is unable to uncover such dependency. However, our algorithm may nonetheless be used as an indirect method to compute an average value of the sheath potential. The total pressure calculated using the pressure balance (Equation (44)) can be evaluated for multiple sheath potentials, and the intersections of the resulting family of pressure curves with the experimental pressure data can be used to estimate the variation of the sheath voltage over the experimental parameter range.

4.2. Comparison to experimental data

We validate the results of our numerical approach to *(i)* experimental wall temperature from both the NSTAR discharge cathode [87] and Salhi's cathode [40] operating on argon at mass flow rates of 0.21 and 0.39 mg/s (0.5 and 0.93 equivalent-amperes, 7 and 13 sccm), *(ii)* experimental measurements of both the electron temperature and attachment length for the latter cathode operating on xenon and for the JPL 1.5 cm LaB$_6$ cathode [22], and *(iii)* measured total pressure for our own hollow cathode, the NSTAR discharge cathode [49, 87] and for the NEXIS cathode [68, 88]. The method by which we obtain the measurement error in both attachment length and electron temperature is shown in [29].

5. Results and discussion

We validate in this section the results of our algorithm for multiple cathodes. The dimensions and operating conditions of each cathode are shown in the Appendix (Table A3). They span a variety of geometries, gases, and operating conditions.

5.1. Wall temperature

We show in Figure 12 a comparison of our model to experimental data of the insert temperature. We applied the algorithm to both Salhi's cathode operating with argon and to the NSTAR cathode. The cathode wall temperature is reported in [40] and [87], respectively. We took the work function from [30] (p.252) for the barium-oxide insert installed in the NSTAR cathode. Salhi's cathode uses a material with an estimated work function of 1.8–2.0 eV [40]. The results from our algorithm are averaged over all of

Physics of Thermionic, Orificed Hollow Cathodes. Part 1: Theory and Experimental Validation 16

the values tested for the two free parameters. We have computed all quantities with sheath voltages and gas temperatures in the range of 1–10 V and 2000–4000 K, respectively. The algorithm returns
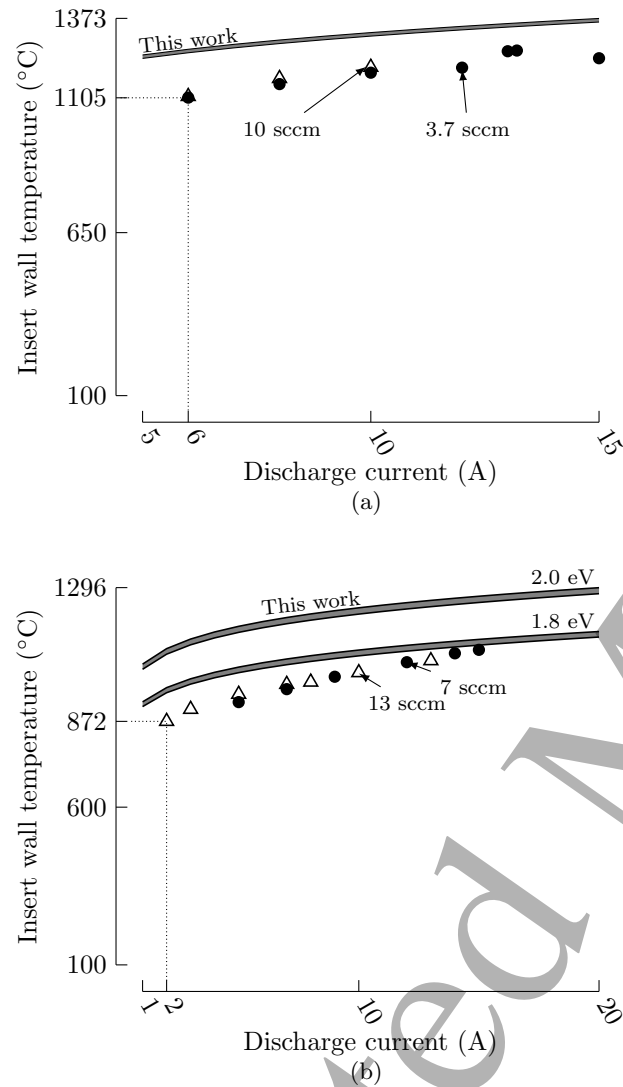

Figure 12: (a) Peak insert temperature of the NSTAR cathode. (b) External wall temperature of Salhi's cathode. Experimental data from [87] and [40], respectively. The reported measurement error is ±15°C for both cathodes. Gray areas on the model indicate the minimum and maximum values obtained for the indicated mass flow rates, with sheath voltage and gas temperature with values between 1–10 V and 2000–4000 K, respectively. Reproduced from "Pierre-Yves C. R. Taunay, *Scaling Laws in Orificed Thermionic Hollow Cathodes,* Ph.D. dissertation, Princeton University, 2020." [23] Copyright 2020, Pierre-Yves C. R. Taunay.

values within 10% of the experimental values for both

cathodes. We find that the trend of the predicted wall temperature agrees with the experimental data, both with increasing discharge current and mass flow rate, which suggests that the scaling of the return ion and electron fluxes is likely captured within the range of sheath potentials considered. Although the scaling is likely captured, we caution that, because of the exponential dependence of the random electron flux (i.e, the electron return current) on the sheath voltage and electron temperature, both errors in the estimation of those quantities and the assumption of volume-averaged quantities can lead to large variations in the plasma parameters within the volume considered.

We also applied the algorithm to Friedly's cathode [36] with an estimated work function of 2 eV for the insert material (as reported in [32], p.91). We found the calculated results to be within 20% of experimental data, but did not have the same agreement as that of the NSTAR. The temperatures reported by Friedly [36] are that of the exterior of the cathode and are higher than the typical application range of barium-based emitters. We hypothesize that the emitter depleted its coating, especially at higher discharge currents, which would explain the reported high temperatures. The uncertainty in the work function of the material would explain the discrepancy observed between the results of the model and the experimental measurements. We found that the observed trend of the results of the algorithm agrees with experimental results if we assume that the work function is equal to 4.1 eV. This value is within the range of the work function of tantalum (4.0–4.8 eV) [89]. Additionally, the assumptions made in [29] to estimate the emission length become invalid at high discharge currents for this particular cathode. The calculated ionization fraction is indeed large in both the orifice (up to 60%) and in the insert (up to 30%) at high discharge currents and therefore challenges the assumption of charge-exchange-dominated ambipolar diffusion. A possible remedy is to include *all* interactions between particles when considering ambipolar diffusion.

5.2. Electron temperature and attachment length

The predicted and experimental attachment length and insert electron temperature are shown in Figure 13a and Figure 13b, respectively. Results are presented for the JPL's 1.5 cm LaB$_6$ hollow cathode [22] operating on xenon at a mass flow rate 0.78 and 1.2 mg/s (8 and 12 sccm) and for Salhi's cathode [40] operating on xenon at a mass flow rate of 0.68 mg/s (0.5 equivalent-amperes, 7 sccm) and with an orifice diameter of 1.21 mm. The insert electron temperature for the JPL's cathode is reported at the location of peak insert electron density. We use the highest reported values for Salhi's cathode, close to the peak insert electron

Physics of Thermionic, Orificed Hollow Cathodes. Part 1: Theory and Experimental Validation   17
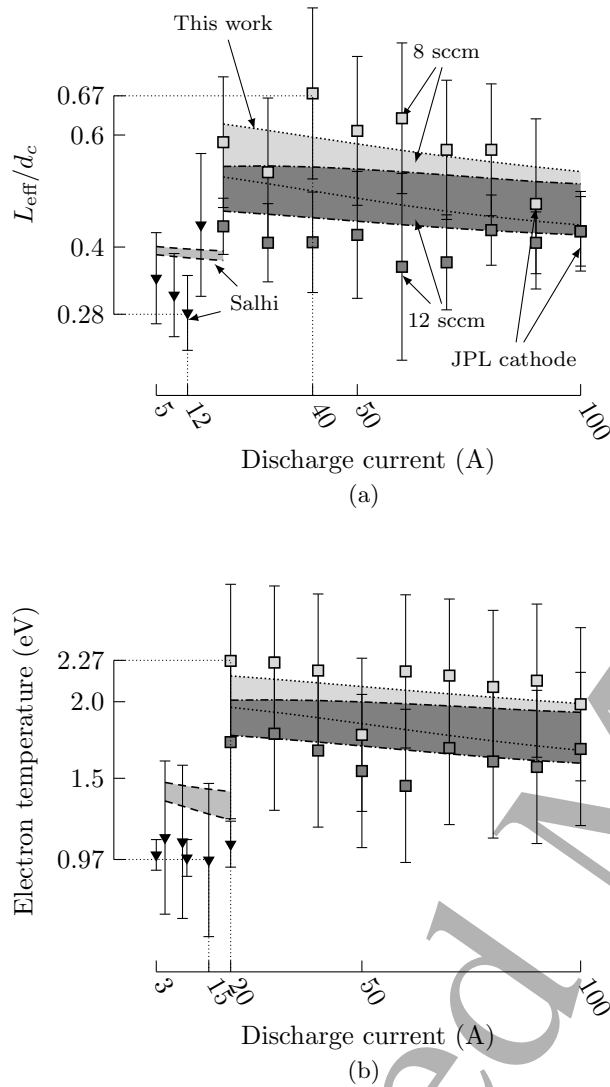
density.

(a)

(b)

Figure 13: (a) Attachment length normalized by the cathode diameter and (b) electron temperature as functions of discharge current. The experimental data for the JPL LaB$_6$ cathode operating at 8 and 12 sccm and for Salhi's cathode operating at 7 sccm are taken from [22] and [40], respectively. Gray areas on the model indicate the minimum and maximum values obtained for the indicated cathodes, with sheath voltage and gas temperature with values between 1– 10 V and 2000–4000 K, respectively. Adapted from "Pierre-Yves C. R. Taunay, *Scaling Laws in Orificed Thermionic Hollow Cathodes,* Ph.D. dissertation, Princeton University, 2020." [23] Copyright 2020, Pierre-Yves C. R. Taunay.

We observe in all cases that the trend of decreasing electron temperature with increasing discharge current

and mass flow rate is correctly captured. The electron temperature is over-predicted in some instances, which is a consequence of an under-prediction of the neutral density and is consistent with an under-predicted neutral gas pressure.

5.3. Pressure

We now compare the prediction of the total pressure inside hollow cathodes from existing models to that from ours for the NSTAR, NEXIS, and our own cathode. The other models are delineated in [37]. For the NSTAR cathode we also perform a comparison with results of a 2-D axisymmetric solver from [49]. For all cathodes, the results are computed with a gas temperature of 3,000 K and sheath voltages between 1 and 10 V. Results are shown in Figure 14. Pressures predicted with both our theoretical model and the empirical correlation derived from literature data from [37] vary with discharge current and mass flow rate, while other existing models do not. These two approaches yield results that are close to the experimentally measured pressure. Results for the NSTAR are similar to that of the 2-D axisymmetric solver, although the latter uses a discharge current 10% higher than the nominal current of 12 A. For cathodes that reasonably satisfy the model assumptions, the numerical algorithm allows us to bound the pressure for a cathode for which no pressure data are available. The algorithm however overestimates the pressure for our cathode. We hypothesize that:

- the magnetic pressure is overestimated because we did not take into account the net current of charged particles from the insert volume directed towards the orifice plate,

- gas leaks occur through the grafoil seals at graphite/stainless steel interfaces at high temperatures, thus decreasing the experimentally measured pressure, or

- gas leaks occur through the NPT fittings on the feed lines and pressure tap because they are sealed only with anti-seize compound as typical thread sealant compounds would not tolerate the operating temperature of the PLHC.

In all cases, knowledge of the sheath potential is required. For a wide range of sheath potentials (1– 10 V), the pressure varies by at most a factor of 2–3. The family of curves generated by the model intersect experimental data at different sheath voltages. As mentioned in the previous section (Section 4.1.2), this may be used to compute the sheath voltage from the experimental data.

Physics of Thermionic, Orificed Hollow Cathodes. Part 1: Theory and Experimental Validation 18

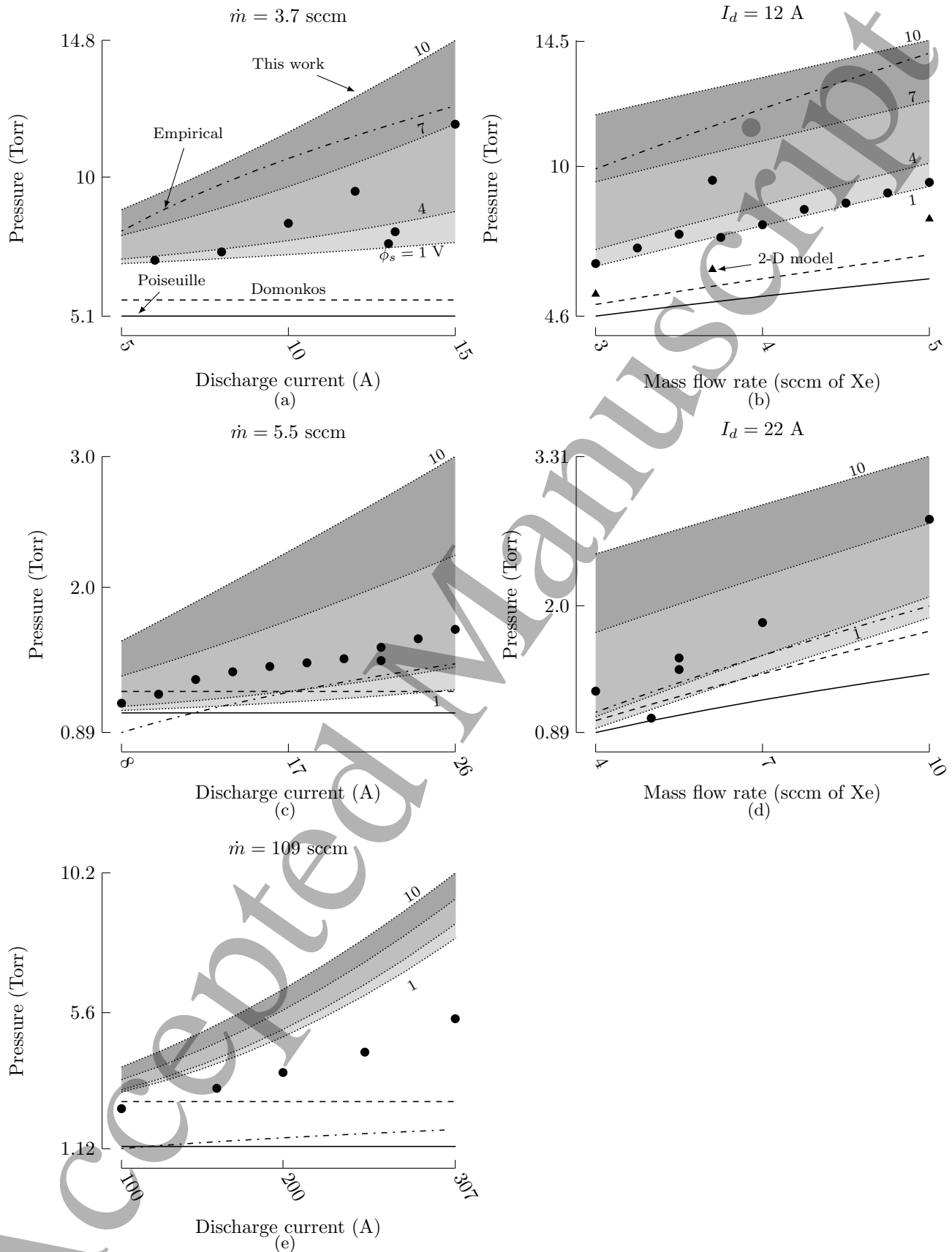Figure 14: Comparison of pressure models used for the calculation of the total pressure inside hollow cathodes. (a,b) NSTAR cathode. Experimental data from [49, 74, 87]. (c,d) NEXIS cathode. Experimental data from [68, 88]. (e) PLHC. Adapted from "Pierre-Yves C. R. Taunay, *Scaling Laws in Orificed Thermionic Hollow Cathodes,* Ph.D. dissertation, Princeton University, 2020." [23] Copyright 2020, Pierre-Yves C. R. Taunay.

6. Conclusion

Based on the lessons learned in our review of prior cathode modeling efforts [28], we have developed a hybrid model for orificed hollow cathodes and computed volume-averaged plasma quantities for a large variety of cathodes and operating conditions. Good agreement is obtained with both literature data and with experimental pressure data we gathered on our own large hollow cathode running on argon at up to 307 A of discharge current.

We were able to bound both the sheath potential and neutral gas temperature and found that the calculated quantities are not sensitive to these parameters. These two parameters can be self-consistently incorporated into the model through a potential solver and the energy equation for the heavy particles, respectively. The values for the neutral gas temperature and sheath potential remain to be experimentally validated. Another possible area of improvement of the model is a better estimation of the static pressure at the orifice outlet. While we have used empirical correlations to obtain scaling relationships and overall trends, 2-D DSMC simulations could provide better accuracy.

This work can be used in conjunction with the charge-exchange-dominated ambipolar diffusion model for the insert region we presented in [29] to find the electron density distribution within a hollow cathode. The model is also a building block for insert performance prediction if coupled to an erosion model for the thermionic material and for cathode performance prediction if coupled to a cathode thermal and plume model. Finally, the proposed model may be used to study scaling laws for hollow cathodes; we perform this analysis in the following paper.

Data availability

The data and software that support the findings of this study are openly available "cathode-database, An open database of thermionic orificed hollow cathode data" at https://doi.org/10.5281/zenodo.3956853 (cathode experimental data and software to assemble the corresponding database) [90], "cathode-package, Python package of cathode models" at https://doi.org/10.5281/zenodo.4592503 (Python package of cathode models, including the one described herein) [91], and "physics-of-cathodes" at https://doi.org/10.5281/zenodo.4615625 (numerical data generated and software used to create the numerical data presented in this paper) [92].

Physics of Thermionic, Orificed Hollow Cathodes. Part 1: Theory and Experimental Validation   20

Appendix

Appendix A.1. Correlation coefficients

Table A1: The coefficients used for the insert electron temperature and attachment length correlations (Equations $(25a)$ and (26)).

Species	Quantity	Index		
		0	1	2
Xe	T_{eV}	1.20072	0.35592	0.52523
	L_{eff}	0.72389	0.17565	1.22140
Ar	T_{eV}	1.66426	0.38159	1.12521
	L_{eff}	0.71827	0.34198	1.19716

Table A2: The coefficients used for the orifice electron temperature (Equation $(25b)$).

Species	Temperature	Index			
		0	1	2	3
Xe	2000 K	1.230	-0.0052	0.313	0.429
	3000 K	1.290	-0.0062	0.337	0.503
	4000 K	1.300	-0.0068	0.365	0.591
Ar	2000 K	1.889	-0.0197	0.287	0.793
	3000 K	1.941	-0.0250	0.320	0.935
	4000 K	1.723	-0.0257	0.401	1.250

Appendix A.2. Cathodes studied

Table A3 lists the cathodes and range of operating conditions that we used for this work and the next paper. For some of the cathodes, we note that operating conditions that are different from the ones reported in Table A3 exist (*e.g.*, Salhi's cathode also has a 1.27 mm diameter orifice). However, we could not gather relevant experimental data (total pressure, attachment length, electron temperature) for those cases. Because of the difficulty of gathering reliable cathode dimension data, we report all of the possible dimensions in Table A4. In both tables, the following abbreviations are used:

- *L.*: Length
- *I.D.*: Inner Diameter
- *O.D.*: Outer Diameter

Physics of Thermionic, Orificed Hollow Cathodes. Part 1: Theory and Experimental Validation   21

Table A3: Dimensions and operating conditions of the benchmark cathodes.

| Cathode | Dimension (mm) | | | | | Species | Mass flow (sccm) | Current (A) | Pressure (Torr) | Refs. for data |
| | Insert | | | Orifice | | | | | | |
	L.	I.D.	O.D.	L.	D.					
Siegfried and Wilbur	25.4	3.9 3.8	4.0	1.8	0.76 0.76	Hg Ar, Xe	$0.35 - 1.42$ $0.8 - 8.0$	$1.27 - 4.3$ $1.24 - 4.3$	$1.3 - 6.2$ $1.8 - 16.6$	[32, 93, 94]* [35]
Friedly	13.0	4.7	N/A	1.0†	0.74	Xe	$2.51 - 6.41$	$5.0 - 60.0$	$5.9 - 52.7$	[36]
Salhi	25.4	3.81	5.53	1.24	0.76, 1.21 1.21	Ar Xe	$0.5 - 1.24$ $0.5 - 0.93$	$1.0 - 20.0$	$4.8 - 25.3$ $6.5 - 14.7$	[40]
AR3 EK6 SC012	25.4	1.22 1.17 1.8	2.29 3.8	0.38 0.71 0.5	0.13	Xe 4.8	$1.40 - 2.40$ $0.8 - 3.25$ $0.57 - 2.44$	1.0 $0.5 - 1.5$	$250.4 - 345.6$ $270.2 - 609.4$ $163.7 - 506.1$	[43]
T6	20.0	2	5	2	1	Xe	$0.51 - 11.5$	$5 - 15$	$6.4 - 41.1$	[69, 95]
NSTAR	25.4	3.8	4.3	0.74	1.02	Xe	$2.47 - 10$	$5.95 - 15$	$4.0 - 27.5$	[49, 74, 87]
NEXIS	25.4	12.7‡	14.2§	0.74¶	2.5, 2.75, 3.0	Xe	$4 - 10$	$4 - 32$	$0.66 - 2.76$	[47, 68, 88]
JPL-1.5cm	25.4	7	13	1.0†	3.8 3, 5	Xe	$8 - 12$ $10.5 - 19.8$	$20 - 100$ $8.9 - 35.1$	$1.9 - 2.6$ $2.4 - 3.4$	[22] [21]
PLHC	80.4	27.15	31.2	1.5	5.6	Ar	109	$100 - 307$	$2.44 - 5.4$	This work

*See [32] pp.17–18 and p.139 for the dimensions and orifice length.
†The orifice length is not specified for those cathodes. It is set to 1.0 mm.
‡We follow later work by Goebel and Katz [30] where the insert diameter is set to 1.27 cm. However, the insert inner diameter has also been suggested to be equal to 1.20 cm in [47, 48, 96].
§The outer diameter for the NEXIS cathode is deduced from insert thickness data retrieved from [47] and [48].
¶Measured from plots in [48].

Table A4: Comprehensive list of dimensions (in mm) of the benchmark cathodes.

| Cathode | Insert | | | Orifice | | Tube | Species | Refs. |
	L	I.D.	O.D.	L	D	D		
Siegfried	25.4	1.9, 3.8, 3.9	4.0	1.8	0.51, 0.76, 0.79, 0.96	0.63	Ar, Hg, Xe	[31, 32, 34, 35, 38, 93, 94]
Friedly	13.0	4.7, 6.4	N/A	N/A	$0.74 - 1.70$	6.4, 12.8	Xe	[36]
Salhi	25.4	3.81	5.53	1.24	0.76, 1.21, 1.27	6.35	Ar, Xe	[40]
AR3 EK6 SC012	25.4	1.22 1.17 1.8	2.29 3.8	0.38 0.71 0.5	0.13	3.18 4.8	Xe	[43]
T6	20.0	2	5	2	0.75, 1.0, 1.3, 1.6	7	Xe	[69, 95, 97]
NSTAR	25.4	3.8	4.3	0.74	1.02	6.35	Xe	[30, 48, 63, 98–101]
NEXIS	25.0, 25.4	12.0, 12.7	N/A	N/A	1.5, 2.0, 2.5, 2.75, 3.0	15	Xe	[30, 47, 48, 75, 88, 96, 98]
JPL-1.5cm	25.4	7	13	N/A	3, 3.8, 5	15	Xe	[22, 102, 103]
PLHC	80.4	27.15	31.2	1.5	5.6	36.2	Ar	This work

Physics of Thermionic, Orificed Hollow Cathodes. Part 1: Theory and Experimental Validation 22

References

[1] Kuo, Y. S., Bunshah, R. F., and Okrent, D., "Hot hollow cathode and its applications in vacuum coating: A concise review," *Journal of Vacuum Science and Technology A*, Vol. 4, No. 397, 1986.

[2] Lunk, A., "Plasma activated physical vapour deposition (PAPVD) by hollow cathode arc (HCA)," *Vacuum*, Vol. 41, No. 7–9, 1990, pp. 1965–1967.

[3] Morgner, H., Neumann, M., Straach, S., and Krug, M., "The hollow cathode: a high-performance tool for plasma-activated deposition," *Surface and Coatings Technology*, Vol. 108–109, 1998, pp. 513–519.

[4] Forrester, A. T., Goebel, D. M., and Crow, J. T., "IBIS: A hollow-cathode multipole boundary ion source," *Applied Physics Letters*, Vol. 33, No. 1, 1978, pp. 11–13.

[5] Tanaka, S., Morita, H., and Sakuraba, J., "Use of a hollow cathode in a duoPIGatron hydrogen ion source," *Japanese Journal of Applied Physics*, Vol. 19, No. 9, 1980, pp. 1703.

[6] Deichuli, P. P., Abdrashitov, G. F., Ivanov, A. A., Kolmogorov, V. V., Mishagin, V. V., Shul'zhenko, G. I., Stupishin, N. V., Beals, D., and Granetz, R., "Ion source with LaB_6 hollow cathode for a diagnostic neutral beam injector," *Review of Scientific Instruments*, Vol. 77, No. 3, 2006, pp. 03B514.

[7] Szabo, J. J., Pote, B., Tedrake, R., Paintal, S., Byrne, L., Hruby, V. J., Kamhawi, H., and Smith, T., "High throughput 600 watt Hall effect thruster for space exploration," 52nd *AIAA/SAE/ASEE Joint Propulsion Conference & Exhibit*, 2016, AIAA-2016-4830.

[8] Brophy, J. R., "NASA's Deep Space 1 ion engine," *Review of Scientific Instruments*, Vol. 73, No. 2, 2002, pp. 1071–1078.

[9] Dodson, C. A., Perez-Grande, D., Jorns, B. A., Goebel, D. M., and Wirz, R. E., "Ion heating measurements on the centerline of a high-current hollow cathode plume," *Journal of Propulsion and Power*, Vol. 34, No. 5, 2018, pp. 1225–1234.

[10] Goebel, D. M. and Chu, E., "High Current Lanthanum Hexaboride Hollow Cathodes for High Power Hall Thrusters," 32nd *International Electric Propulsion Conference*, 2011, IEPC-2011-053.

[11] Hofer, R., Randolph, T., Oh, D., Snyder, J., and de Grys, K., "Evaluation of a 4.5 kW Commercial Hall Thruster System for NASA Science Missions," 42nd *AIAA/ASME/SAE/ASEE Joint Propulsion Conference & Exhibit*, 2006, AIAA-2006-4469.

[12] Brown, D. L., Beal, B. E., and Haas, J. M., "Air Force Research Laboratory High Power Electric Propulsion Technology Development," *IEEE Aerospace Conference*, 2010.

[13] Hall, S. J., Jorns, B. J., Gallimore, A. D., Kamhawi, H., Haag, T. W., Mackey, J. A., Gilland, J. H., Peterson, P. Y., and Baird, M., "High-power performance of a 100-kW class nested Hall thruster," 35th *International Electric Propulsion Conference*, 2017, IEPC-2017-228.

[14] Jorns, B., Gallimore, A. D., Hall, S. J., Peterson, P. Y., Gilland, J. E., Goebel, D. M., Hofer, R., and Mikellides, I., "Update on the Nested Hall Thruster Subsystem for the NextSTEP XR-100 Program," *AIAA Propulsion and Energy Forum*, 2018, AIAA-2018-4418.

[15] Shark, S. W., Hall, S. J., Jorns, B., Hofer, R. R., and Goebel, D., "High Power Demonstration of a 100 kW Nested Hall Thruster System," *AIAA Propulsion and Energy*, 2019, AIAA-2019-3809.

[16] Shastry, R., Herman, D. A., Soulas, G. C., and Patterson, M. J., "Status of NASA's Evolutionary Xenon Thruster (NEXT) Long-Duration Test as of 50,000 h and 900 kg Throughput," 33rd *International Electric Propulsion*

Conference, 2013, IEPC-2013-121.

[17] Polk, J. E., Capece, A. M., and Mikellides, I. G., "Barium Depletion in the NSTAR Discharge Cathode After 30,472 Hours of Operation," 46th *AIAA/ASME/SAE/ASEE Joint Propulsion Conference & Exhibit*, 2010, AIAA-2010-6702.

[18] Ohkawa, Y., Higuchi, T., Hayakawa, Y., Miyazaki, K., and Nagano, H., "Observation and Analysis of Graphite Hollow Cathode after 45,000-Hour Life Test," 33rd *International Electric Propulsion Conference*, 2013, IEPC-2013-364.

[19] van Noord, J. L., Kamhawi, H., and McEwen, H. K., "Characterization of a High Current, Long Life Hollow Cathode," Tech. Rep. TM-214095, NASA, 2006.

[20] Goebel, D. M. and Chu, E., "High Current Lanthanum Hexaboride Hollow Cathode for High-Power Hall Thrusters," *Journal of Propulsion and Power*, Vol. 30, No. 1, 2014.

[21] Becatti, G., Goebel, D. M., Polk, J. E., and Guerrero, P., "Life Evaluation of a Lanthanum Hexaboride Hollow Cathode for High-Power Hall Thruster," *Journal of Propulsion and Power*, Vol. 34, No. 4, 2017, pp. 893–900.

[22] Chu, E. and Goebel, D. M., "High-current lanthanum hexaboride hollow cathode for 10-to-50-kW hall thrusters," *IEEE Transactions on Plasma Science*, Vol. 40, No. 9, 2012, pp. 2133–2144.

[23] Taunay, P.-Y. C. R., *Scaling Laws in Orificed Thermionic Hollow Cathodes*, Ph.d., Princeton University, 2020.

[24] Leung, K., Pincosy, P., and Ehlers, K., "Directly heated lanthanum hexaboride filaments," *Review of scientific instruments*, Vol. 55, No. 7, 1984, pp. 1064–1068.

[25] Doerner, R., Tynan, G., Oyerzabal, E., Taylor, K., Goebel, D., and Katz, I., "Plasma Surface Interaction Studies for Next-Generation Ion Thrusters," 40th *AIAA/ASME/SAE/ASEE Joint Propulsion Conference & Exhibit*, 2004, AIAA-2004-4104.

[26] Goebel, D. M., Jameson, K. K., and Hofer, R. R., "Hall thruster cathode flow impact on coupling voltage and cathode life," *Journal of Propulsion and Power*, Vol. 28, No. 2, 2012, pp. 355–363.

[27] Goebel, D. M., Becatti, G., Mikellides, I. G., and Lopez Ortega, A., "Plasma hollow cathodes," *Journal of Applied Physics*, Vol. 130, No. 5, 2021, pp. 050902.

[28] Wordingham, C. J., Taunay, P.-Y. C. R., and Choueiri, E. Y., "A Critical Review of Orificed Hollow Cathode Modeling: 0-D Models," 53rd *AIAA/SAE/ASEE Joint Propulsion Conference & Exhibit*, 2017, AIAA-2017-4888.

[29] Wordingham, C. J., Taunay, P.-Y. C. R., and Choueiri, E. Y., "The Attachment Length in Orificed Hollow Cathodes," *Plasma Sources Science and Technology*, 2021, In press.

[30] Goebel, D. and Katz, I., *Fundamentals of Electric Propulsion: Ion and Hall Thrusters*, John Wiley & Sons, Inc., 2008.

[31] Siegfried, D. E. and Wilbur, P. J., "Studies on an experimental quartz tube hollow cathode," 14th *International Electric Propulsion Conference*, 1979, AIAA-1979-2056.

[32] Siegfried, D. E., *A Phenomenological Model for Orificed Hollow Cathodes*, Ph.D., Colorado State University, 1982.

[33] Siegfried, D. E. and Wilbur, P. J., "Phenomenological Model Describing Orificed, Hollow Cathode Operation," *AIAA Journal*, Vol. 21, No. 1, 1983, pp. 5–6.

[34] Siegfried, D. E. and Wilbur, P. J., "A model for mercury orificed hollow cathodes - Theory and experiment," *AIAA Journal*, Vol. 22, No. 10, 1984, pp. 1405–1412.

[35] Wilbur, P. J., "Advanced Ion Thruster Research," Tech.

Rep. CR-168340, NASA, 1984.

[36] Friedly, V. J., "Hollow Cathode Operation at High Discharge Currents," 1990, M.Sc.

[37] Taunay, P.-Y. C. R., Wordingham, C. J., and Choueiri, E. Y., "An Empirical Scaling Relationship for the Total Pressure in Hollow Cathodes," *AIAA Propulsion and Energy Forum*, 2018, AIAA-2018-4428.

[38] Siegfried, D. E. and Wilbur, P. J., "An investigation of mercury hollow cathode phenomena," *13th International Electric Propulsion Conference*, 1978.

[39] Salhi, A. and Turchi, P. J., "Theoretical Modeling of Orificed Hollow Cathode Discharges," *23rd International Electric Propulsion Conference*, 1993, IEPC-1993-024.

[40] Salhi, A., *Theoretical and experimental studies of orificed, hollow cathode operation*, Ph.D., The Ohio State University, 1993.

[41] Mizrahi, J. P., Vekselman, V., Krasik, Y., and Gurovich, V., "0-D Plasma Model for Orificed Hollow Cathodes," *32nd International Electric Propulsion Conference*, 2011, IEPC-2011-334.

[42] Mizrahi, J., Vekselman, V., Gurovich, V., and Krasik, Y. E., "Simulation of Plasma Parameters During Hollow Cathodes Operation," *Journal of Propulsion and Power*, Vol. 28, No. 5, 2012, pp. 1134–1137.

[43] Domonkos, M. T., *Evaluation of low-current orificed hollow cathodes*, Ph.D., University of Michigan, 1999.

[44] Domonkos, M. T., "A Particle and Energy Balance Model of the Orificed Hollow Cathode," *38th AIAA/ASME/SAE/ASEE Joint Propulsion Conference & Exhibit*, 2002, AIAA-2002-4240.

[45] Albertoni, R., *Cathode Processes in MPD Thrusters*, Ph.D., Universita Degli Studi di Pisa, 2012.

[46] Albertoni, R., Pedrini, D., Paganucci, F., and Andrenucci, M., "A Reduced-Order Model for Thermionic Hollow Cathodes," *IEEE Transactions on Plasma Science*, Vol. 41, No. 7, 2013, pp. 1731–1745.

[47] Mikellides, I. G., Katz, I., Goebel, D. M., and Polk, J. E., "Hollow cathode theory and experiment. II. A two-dimensional theoretical model of the emitter region," *Journal of Applied Physics*, Vol. 98, 2005, pp. 113303.

[48] Mikellides, I. G., Katz, I., Goebel, D. M., Polk, J. E., and Jameson, K. K., "Plasma processes inside dispenser hollow cathodes," *Physics of Plasmas*, Vol. 13, 2006.

[49] Mikellides, I. G., "Effects of Viscosity in a Partially Ionized Channel Flow with Thermionic Emission," *Physics of Plasmas*, Vol. 16, 2009, pp. 013501.

[50] Mikellides, I. G., Goebel, D. M., Jorns, B. a., Polk, J. E., and Guerrero, P., "Numerical Simulations of the Partially-ionized Gas in a 100-A LaB$_6$ Hollow Cathode," *IEEE Transactions on Plasma Science*, Vol. 43, No. 1, 2015, pp. 1–15.

[51] Sary, G., Garrigues, L., and Boeuf, J.-P., "Hollow cathode modeling: I. A coupled plasma thermal two-dimensional model," *Plasma Sources Science and Technology*, Vol. 26, No. 5, 2017, pp. 55007.

[52] Sary, G., Garrigues, L., and Boeuf, J.-P., "Hollow cathode modeling: II. Physical analysis and parametric study," *Plasma Sources Science and Technology*, Vol. 26, No. 5, 2017, pp. 055008.

[53] Guerrero, P., Mikellides, I. G., Polk, J. E., Carmina Monreal, R., and Meiron, D. I., "Critical implications of ion-surface energy accommodation and neutralization mechanism in hollow cathode physics," *Journal of Applied Physics*, Vol. 130, No. 4, 2021, pp. 043306.

[54] Kubota, K., Oshio, Y., Watanabe, H., Cho, S., Ohkawa, Y., and Funaki, I., "Hybrid-PIC Simulation on Plasma Flow of Hollow Cathode," *34th International Electric Propulsion Conference*, 2015, IEPC-2015-15.

[55] Kubota, K., Oshio, Y., Watanabe, H., Cho, S., Ohkawa, Y., and Funaki, I., "Hybrid-PIC Simulation

of LaB6 Hollow Cathode Self-Heating Characteristics," *TRANSACTIONS OF THE JAPAN SOCIETY FOR AERONAUTICAL AND SPACE SCIENCES*, Vol. 62, No. 1, 2019, pp. 11–19.

[56] Cao, S., Ren, J., Tang, H., Zhang, Z., Wang, Y., Cao, J., and Chen, Z., "Numerical simulation of plasma power deposition on hollow cathode walls using particle-in-cell and Monte Carlo collision method," *Physics of Plasmas*, Vol. 25, No. 10, 2018.

[57] Cao, S., Ren, J., Tang, H., Pan, R., Zhang, Z., Zhang, K., and Cao, J., "Modeling on plasma energy balance and transfer in a hollow cathode," *Journal of Physics D: Applied Physics*, Vol. 52, No. 28, 2019, pp. 285202.

[58] Mandell, M. J. and Katz, I., "Theory of Hollow Cathode Operation in Spot and Plume Modes," *30th AIAA/ASME/SAE/ASEE Joint Propulsion Conference & Exhibit*, 1994, AIAA-1994-3134.

[59] Katz, I., Gardner, B., Jongeward, G., Patterson, M., and Myers, R., "A model of plasma contactor behavior in the laboratory," *34th Aerospace Sciences Meeting & Exhibit*, 1996, AIAA-1996-0484.

[60] Katz, I., Gardner, B M., Mandell, M. J., Jongeward, G. A., Patterson, M., and Myers, R. M., "Model of Plasma Contactor Performance," *Journal of Spacecraft and Rockets*, Vol. 34, No. 6, 1997.

[61] Katz, I., Mandell, M. J., Patterson, M., and Domonkos, M., "Sensitivity of Hollow Cathode Performance to Design and Operating Parameters," *35th AIAA/ASME/SAE/ASEE Joint Propulsion Conference & Exhibit*, 1999, AIAA-1999-2576.

[62] Capacci, M., Minucci, M., and Severi, A., "Simple numerical model describing discharge parameters in orificed hollow cathode devices," *33rd AIAA/ASME/SAE/ASEE Joint Propulsion Conference & Exhibit*, 1997, AIAA-1997-2791.

[63] Katz, I., Anderson, J. R., Polk, J. E., and Brophy, J. R., "One-Dimensional Hollow Cathode Model," *Journal of Propulsion and Power*, Vol. 19, No. 4, 2003, pp. 595–600.

[64] Pedrini, D., Albertoni, R., Paganucci, F., and Andrenucci, M., "Theoretical Model of a Lanthanum Hexaboride Hollow Cathode," *IEEE Transactions on Plasma Science*, Vol. 43, No. 1, 2015.

[65] Pedrini, D., Cannelli, F., Ducci, C., Misuri, T., Paganucci, F., and Andrenucci, M., "Hollow Cathodes Development at SITAEL," *Space Propulsion*, 2016.

[66] Wordingham, C. J., Taunay, P.-Y. C. R., and Choueiri, E. Y., "Multi-kilowatt Class Heaters for Large Hollow Cathodes," *Review of Scientific Instruments*, Vol. 87, No. 7, 2018.

[67] Brown, J., "Design and Implementation of an Actuated Probe Suite for an Orificed Hollow Cathode," B.Sc. Thesis, 2018, Princeton University.

[68] Jameson, K. K., Goebel, D. M., and Watkins, R. M., "Hollow Cathode and Thruster Discharge Chamber Plasma Measurements Using High-Speed Scanning Probes," *29th International Electric Propulsion Conference*, 2005, IEPC-2005-269.

[69] Patterson, S. W. and Fearn, D. G., "The Generation of High Energy Ions in Hollow Cathode Discharges," *26th International Electric Propulsion Conference*, 1999, pp. 695–702, IEPC-1999-125.

[70] Katz, I., Anderson, J., Polk, J., and Brophy, J., "A Model of Hollow Cathode Plasma Chemistry," *38th AIAA/ASME/SAE/ASEE Joint Propulsion Conference & Exhibit*, 2002, AIAA-2002-4241.

[71] Gurciullo, A., Fabris, A. L., and Potterton, T., "Numerical study of a hollow cathode neutraliser by means of a zero-dimensional plasma model," *Acta Astronautica*, Vol. 174, 2020, pp. 219–235.

Physics of Thermionic, Orificed Hollow Cathodes. Part 1: Theory and Experimental Validation 24

[72] Jobson, D. A., "On the flow of a compressible fluid through orifices," *Proceedings of the Institution of Mechanical Engineers*, Vol. 169, No. 1, 1955, pp. 767–776.

[73] Prewett, P. and Allen, J., "The double sheath associated with a hot cathode," *Proceedings of the Royal Society of London A: Mathematical, Physical and Engineering Sciences*, Vol. 348, The Royal Society of London, 1976, pp. 435–446.

[74] Jameson, K. K., Goebel, D. M., and Watkins, R. M., "Hollow Cathode and Keeper-Region Plasma Measurements," *41st AIAA/ASME/SAE/ASEE Joint Propulsion Conference & Exhibit*, 2005, AIAA-2005-3667.

[75] Goebel, D. M., Jameson, K. K., Watkins, R. M., Katz, I., and Mikellides, I. G., "Hollow cathode theory and experiment. I. Plasma characterization using fast miniature scanning probes," *Journal of Applied Physics*, Vol. 98, No. 11, 2005.

[76] Jahn, R. G., *Physics of Electric Propulsion*, Dover Publications, 2006, p. 244.

[77] Taunay, P.-Y. C. R., Wordingham, C. J., and Choueiri, E. Y., "Open electric propulsion with an application to thermionic orificed hollow cathodes," *AIAA Propulsion and Energy Forum*, 2020, AIAA-2020-3638.

[78] Santeler, D. J., "Exit loss in viscous tube flow," *Journal of Vacuum Science & Technology A: Vacuum, Surfaces, and Films*, Vol. 4, No. 3, 1986, pp. 348–352.

[79] Livesey, R. G., *Foundations of Vacuum Science and Technology*, chap. Flow of Gases Through Tubes and Orifices, John Wiley & Sons, Inc, 1998, pp. 135–137.

[80] Cassady, L., *Lithium-fed Arc Multichannel and Single-Channel Hollow Cathode: Experiment and Theory*, Ph.D., Princeton University, 2006, pp.105–110.

[81] Jitschin, W., Ronzheimer, M., and Khodabakhshi, S., "Gas flow measurement by means of orifices and Venturi tubes," *Vacuum*, Vol. 53, No. 1-2, 1999, pp. 181–185.

[82] Sharipov, F., "Numerical simulation of rarefied gas flow through a thin orifice," *Journal of Fluid Mechanics*, Vol. 518, 2004, pp. 35.

[83] Chen, F. F., *Introduction to plasma physics and controlled fusion*, Springer Science, 2006.

[84] Lieberman, M. A. and Lichtenberg, A. J., *Principles of Plasma Discharges and Materials Processing*, Wiley Interscience, 2005.

[85] Hayashi, M., "Bibliography of Electron and Photon Cross Sections with Atoms and Molecules Published in the 20th Century - Xenon," Tech. Rep. NIFS-DATA-79, NIFS, 2003.

[86] "Hayashi database," http://www.lxcat.net, Retrieved in March, 2021.

[87] Polk, J., Grubisic, A., Taheri, N., Goebel, D. M., and Hornbeck, S. E., "Emitter Temperature Distributions in the NSTAR Discharge Hollow Cathode," *41st AIAA/ASME/SAE/ASEE Joint Propulsion Conference & Exhibit*, 2005, AIAA-2005-4398.

[88] Goebel, D. M. Jameson, K. K. and Katz, I., "Hollow Cathode and Keeper-Region Plasma Measurements Using Ultra-Fast Miniature Scanning Probes," *40th AIAA/ASME/SAE/ASEE Joint Propulsion Conference & Exhibit*, 2004, AIAA-2004-3430.

[89] Rumble, J., editor, *CRC handbook of chemistry and physics*, CRC Press, 100th ed., 2019, p.12-122.

[90] Taunay, P.-Y. C. R., "eppdyl/cathode–database — An open database of thermionic orificed hollow cathode-data," 2020.

[91] Taunay, P.-Y. C. R. and Wordingham, C. J., "eppdyl/cathode-package — Python package of cathode models," 2020.

[92] Taunay, P.-Y. C. R., "pytaunay/physics-of-cathodes," 2021.

[93] Wilbur, P. J., "Ion and Advanced Electric Thruster Research," Tech. Rep. CR-165253, NASA, 1980.

[94] Siegfried, D. E. and Wilbur, P. J., "Phenomenological model describing orificed, hollow cathode operation," *15th International Electric Propulsion Conference*, 1981, AIAA-1981-0746.

[95] Fearn, D. G. and Patterson, S. W., "Characterisation of the high current hollow cathode for the T6 thruster," *34th AIAA/ASME/SAE/ASEE Joint Propulsion Conference & Exhibit*, 1998, AIAA-1998-3346.

[96] Mikellides, I. G., Katz, I., Goebel, D. M., and Polk, J. E., "Model of a Hollow Cathode Insert Plasma," *40th AIAA/ASME/SAE/ASEE Joint Propulsion Conference & Exhibit*, 2004, AIAA-2004-3817.

[97] Patterson, S. W., Jugroot, M., and Fearn, D. G., "Discharge Initiation in the T6 Thruster Hollow Cathode," *36th AIAA/ASME/SAE/ASEE Joint Propulsion Conference & Exhibit*, 2000, AIAA-2000-3532.

[98] Goebel, D. M., Katz, I., Polk, J. E., Mikellides, I. G., Jameson, K. K., Liu, T., and Dougherty, R., "Extending Hollow Cathode Life for Electric Propulsion in Long-Term Missions," *Space Conference & Exhibit*, 2004, AIAA-2004-5911.

[99] Katz, I., Polk, J. E., Mikellides, I. G., Goebel, D. M., and Hornbeck, S. E., "Combined Plasma and Thermal Hollow Cathode Insert Model," *29th International Electric Propulsion Conference*, 2005, IEPC-2005-228.

[100] Mikellides, I. G., Katz, I., Goebel, D. M., Jameson, K. K., and Polk, J. E., "Wear Mechanisms in Electron Sources for Ion Propulsion, II: Discharge Hollow Cathode," *Journal of Propulsion and Power*, Vol. 24, No. 4, 2008, pp. 866–879.

[101] Mikellides, I. G., Katz, I., Goebel, D. M., Jameson, K. K., and Polk, J. E., "Wear Mechanisms in Electron Sources for Ion Propulsion, I: Neutralizer Hollow Cathode," *Journal of Propulsion and Power*, Vol. 24, No. 4, 2008, pp. 855–865.

[102] Goebel, D. M., Watkins, R. M., and Jameson, K. K., "LaB$_6$ Hollow Cathodes for Ion and Hall Thrusters," *Journal of Propulsion and Power*, Vol. 23, No. 3, 2007, pp. 552–558.

[103] Goebel, D. M. and Watkins, R. M., "Compact lanthanum hexaboride hollow cathode," *Review of Scientific Instruments*, Vol. 81, No. 8, 2010, pp. 083504.